Thin–Walled Structures 208 (2025) 112825

Contents lists available at ScienceDirect

Thin-Walled Structures

journal homepage: www.elsevier.com/locate/tws

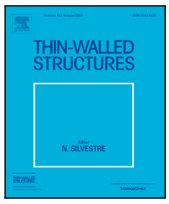

Full length article

# Shell-based finite element model for predicting buckling stability of superelastic structures for elastocaloric cooling

Luka Porenta [a], Boštjan Brank [b], Jaka Tušek [a], Miha Brojan [a,*]

[a] University of Ljubljana, Faculty of Mechanical Engineering, Askerceva 6, SI-1000 Ljubljana, Slovenia
[b] University of Ljubljana, Faculty of Civil and Geodetic Engineering, Jamova 2, SI-1000 Ljubljana, Slovenia

ARTICLE INFO

*Keywords:*
Buckling stability
Shell finite element
Shape memory alloys
Elastocaloric effect
Phase diagram

ABSTRACT

Elastocaloric cooling devices loaded in compression have shown significant potential for fatigue-resistant operation, but for efficient operation they require thin-walled elements to facilitate heat transfer. This can cause elastocaloric elements made of superelastic materials, such as shape memory alloys (SMA), to collapse due to buckling. A common approach for computationally predicting the buckling response of these materials, which exhibit phase transformations during operation, is either to use 3D solid finite elements that can be easily coupled with 3D constitutive equations (which is accurate but extremely time consuming), or to use shell or beam finite elements coupled with simplified constitutive models (which is usually faster but has limited accuracy). In this work, we present a novel numerical approach that combines a highly accurate 7-parameter shell formulation and full 3D constitutive equations that account for the phase transformation between austenite and martensite as well as the compression–tension asymmetry in shape memory alloys (SMA) to study buckling stability. A combination of a perturbation of the structural mesh in the radial direction and a perturbation force was used to model imperfections that triggered the instability processes in the numerical simulations. The numerical responses are compared with experimental observations and show good agreement in terms of stress–strain behavior and buckling modes. Phase diagrams of the buckling modes are numerically determined for tubes with an outer diameter between 2 and 3 mm and a diameter-to-thickness ratio in the range between 5 and 25, which appear to be promising candidates for use in elastocaloric technology. We have thus demonstrated the potential of the proposed computational model as a fast and reliable tool to simulate the buckling and post-buckling behavior of SMA elements not only for elastocaloric technology but also for other applications where superelastic SMA elements are used.

## 1. Introduction

Shape memory alloys (SMAs) are considered smart materials due to their unique properties, i.e., shape memory effect (SME) and superelasticity (SE), both of which are a consequence of first-order martensitic transformation caused by temperature change and/or mechanical loading. More specifically, SME is the ability of the material to recover the original shape after deformation (i.e., temperature-induced transformation), while SE is the ability of a material to withstand (recover) large strains (i.e., stress-induced transformation). The martensitic phase transformation is characterized as a change in the crystal structure of the material from multivariant, low-order, low-temperature martensite to single-variant, high-order, high-temperature austenite, and vice-versa. In the case of stress-induced transformation, the latent heat is absorbed/released from/to the material, and if the mechanical load is applied at high strain rates, this causes temperature changes in the materials, which is called the elastocaloric effect (eCE).

Due to their unique properties, SMAs (among which binary NiTi alloy is the most common) are used in a wide range of applications [1], e.g., for stents and bone implants in medicine [2], as actuators in aerospace industry [3] and robotics [4], and as damping elements in civil engineering [5]. A new potential application field is quickly emerging, namely, elastocaloric cooling and heating. Elastocaloric technology was recognized by the U.S. Department of Energy [6] and later by the European Commission [7] as one of the most promising alternatives to nowadays widely used and environmentally harmful vapor-compression technology. It is based on the cyclic mechanical loading of SMA and the related elastocaloric effect, where released/absorbed latent heat due to phase transformation is effectively used. A typical elastocaloric cycle consists of four steps: (I) adiabatic mechanical loading that heats up the material, (II) heat transfer to the heat sink, (III) adiabatic mechanical unloading that cools down the material, and (IV)

* Corresponding author.
*E-mail address:* miha.brojan@fs.uni-lj.si (M. Brojan).

https://doi.org/10.1016/j.tws.2024.112825
Received 3 July 2024; Received in revised form 7 November 2024; Accepted 9 December 2024
Available online 16 December 2024

heat transfer from the heat source [8]. Over the past decade, about 15 proof-of-the-concept devices have been built, and the best of them have already demonstrated commercially relevant cooling/heating properties [9–18]. The early prototypes (e.g., [9,11,12]) were based on tensile loading of the SMA elements, however, poor fatigue life was exhibited due to rapid crack propagation during tensile cyclic loading [19,20], which prevents practical elastocaloric applications, where several million loading cycles would be required. Compressive loading, on the other hand, provides better fatigue life [21,22], but in return, structural instabilities may occur, such that prevent reversible mechanical loading of SMA and thus reproducible eCE [22]. To design an efficient and powerful elastocaloric device, efficient and rapid heat transfer between the SMA elements and the heat transfer medium (fluid) must be provided. In general, geometries with large specific heat transfer areas per unit volume would provide high(er) heat transfer rates. Thus, thin-walled structures are required for efficient elastocaloric devices. However, thin-walled structures are highly susceptible to buckling in conjunction with compressive loading. Therefore, understanding and predicting the buckling of SMA elements is crucial for finding a compromise between the efficient heat transfer properties of SMA elements on the one hand and a stable structural response on the other. As we have shown in [22], thin-walled tubes seem to be the ideal candidate to achieve this compromise among the geometries currently available on the market, such as tubes, wires, sheets, strips, and rods.

### 1.1. Review of SMA buckling stability studies

To date, a few studies (experimental and numerical) have been conducted on the buckling of SMA elements subjected to axial compressive loading. Initially, the motivation for the studies was a possible application of SMA elements as high-energy absorption dampers, and only recently the studies for elastocaloric cooling purposes have been conducted. In some investigations, solid rods [23–30] and plates [31] were considered, while the majority was focused on tubes with circular cross-section [22,29,32–40].

In experimental studies [32–34], superelastic Ni-Ti tubes of various dimensions underwent dynamic and quasistatic compressive loading. In [34], the experiments were also numerically simulated, using solid 3D finite elements and a simple three-linear SMA material model with neglected compression–tension asymmetry. By changing the geometry of the tube in simulations, a phase diagram of different buckling modes in $D_{out}/t$ - $L_g/D_{out}$ space was obtained as the result. In [29,35], superelastic Ni-Ti tubes of various lengths were subjected to isothermal axial compression loading, where the buckling–unbuckling phenomenon was observed for several dimensions. In this phenomenon, initially, straight elements start to buckle at the beginning of the transformation and then start to straighten at increased axial load, i.e., unbuckle. Further investigations of buckling–unbuckling were performed in [41]. Only a few experimental studies have explored buckling upon cyclic compressive loading, which is crucial for elastocaloric devices. In [22], superelastic Ni-Ti tubes of different lengths were subjected to cyclic compressive loading, aiming to identify stable dimensions and critical buckling stress. Additionally, researchers developed a 1D numerical truss-beam model based on small strain theory and conducted a linear buckling analysis to predict critical buckling loads under various boundary conditions. In our recent study [40], an extensive investigation focused on defining functionally stable lengths of superelastic SMA tubes for elastocaloric technology was performed. The tubes were subjected to an isothermal loading cycle, followed by 50 training cycles and 20 adiabatic cycles (the conditions expected in an elastocaloric device). As a result, phase diagrams of buckling modes with marked regions of functionally stable dimensions and critical buckling stresses for different tube dimensions were obtained.

In numerical investigations, e.g., [36–39], a solid 3D finite elements were primarily employed. More specifically, in [36], the response of a superelastic Ni-Ti tube compressed between two flat surfaces was predicted using a small strain material model that accounts for isothermal transformation and smooth transition from elastic to transformation region while neglecting the compression–tension asymmetry. The work continued in [37] by extending the material model to account for compression–tension asymmetry and plastic deformation of martensite. The researchers showed that the asymmetry has a significant effect on the post-buckling response during loading, while the plastic deformations have the greatest effect on the unloading response of the tube, resulting in a larger hysteresis. In [38], snap buckling of Ni-Ti tubes was investigated numerically. Using a material model based on finite strain theory that accounts for compression–tension asymmetry, the authors first performed a sensitivity analysis of the amplitude of the imperfection, followed by simulations of the experiments [35]. Similarly, the numerical investigation in [39] used the experiments of [35] as a reference and for identifying material parameters. The authors developed a small strain material model that accounts for compression–tension asymmetry, assumes isothermal transformation, and neglects the smooth transition from elastic to transformation region. Their main result is s phase diagram of buckling modes in $D_{out}/t - L_g/D_{out}$ space for undefined $D_{out}$ (authors assumed that geometry can be defined with only two dimensionless parameters). These studies contribute to the understanding of SMA tube behavior under compression, emphasizing the significance of compression–tension asymmetry and imperfections in the buckling analysis.

### 1.2. Aims and scopes

As presented in the previous reviewing paragraphs, numerical simulations of buckling of thin-walled Ni-Ti tubes have almost exclusively used solid 3D finite elements. The numerical description of the buckling response of thin-walled structures based on solid 3D finite elements can be accurate. However, to obtain an accurate solution, a large number of finite elements is required due to multiple layers of mesh in the structure and also in the thickness direction. As a result of using a large number of finite elements, high computational costs are inevitable. On the other hand, shell finite elements are 2D structural elements with reduced thickness dimensions and are, therefore, more suitable for dealing with thin-walled structures. Thus far, the structural stability of thin-walled SMA elements has not been numerically investigated with shell finite elements. In this work, we use our previously developed numerical model based on 7-parameter shell finite elements [42] with implemented 3D constitutive equations [43] to investigate the structural stability of various Ni-Ti tubes and to predict the response of thin-walled Ni-Ti tubes that are subjected to axial compressive loading. The shell finite element is based on large rotations and one-director shell formulation and incorporates assumed natural strain (ANS) and enhanced assumed strain (EAS) concepts. Constitutive equations of SMA are based on small strain theory and consider isothermal transformation as well as compression–tension asymmetry, which is crucial to be taken into account to obtain accurate buckling response of the SMA tubes [36].

The goal of this paper is to demonstrate the effectiveness of shell-based finite elements for the investigation of the buckling stability of superelastic shell structures. A comprehensive experimental validation of the computational model is made by comparing the results of the obtained numerical responses of various axially loaded tubes to those obtained experimentally in [40]. In order to extend the buckling phase diagrams over a wider range of different tubes' geometries and make them more useful for designing tube-based elastocaloric devices, extended phase diagrams of buckling mode shapes in $\lambda$-$D_{out}/t$ space for constant $D_{out}$ and in $\lambda$-$D_{out}$ space for constant $D_{out}/t$ ratio are constructed by adding the computational results also for the tubes that were not tested experimentally. In these simulations, the imperfections are imposed by combining a small random perturbation of the numerical mesh in radial direction and a small lateral perturbation force

that was applied before the axial load. This combination turned out to be very robust and universal. It enabled computations without any pre-knowledge of the shell behavior. By imposing small amplitudes of the imperfections they had practically no influence on the results and, importantly, the same imperfections could be used to incite different buckling modes, all of which comparable to their corresponding experiments.

The rest of the paper is organized in the following way: in Section 2, the numerical model, i.e., 7-parameter shell and constitutive equations, is briefly presented. In Section 3, numerical simulations are presented in detail, including the definition of the considered boundary problem and material parameters identification. Section 4 gathers the results and contains the discussion, while conclusions are drawn in Section 5.

## 2. Numerical model

The numerical model in this work combines 7-parameter shell finite element from our previous works [42,44] and SMA constitutive equations [43] that assume a smooth transition from elastic to transformation region and accounts for compression–tension asymmetry. First, constitutive equations for SMA material model are given, followed by a brief presentation of 7-parameter shell kinematic equations.

### 2.1. Constitutive equations of SMA

Constitutive equations of the material model [43] are based on the following assumptions: (*i*) austenite is an isotropic linearly elastic material, (*ii*) transformation surface has a constant radius that is equal to the height of hysteresis (stress difference) at the uniaxial compressive loading, (*iii*) transformation is isothermal, (*iv*) transformation is considered to be an inelastic component of strain and is incompressible, and (*v*) plastic deformations are neglected.

According to small strain theory, strain tensor $\boldsymbol{E}$ and strain rate tensor $\dot{\boldsymbol{E}}$ are assumed to be additively decomposed into elastic and transformation part:

$$\boldsymbol{E} = \boldsymbol{E}_\mathrm{e} + \boldsymbol{E}_\mathrm{t}, \quad \dot{\boldsymbol{E}} = \dot{\boldsymbol{E}}_\mathrm{e} + \dot{\boldsymbol{E}}_\mathrm{t}. \tag{1}$$

It is assumed that Helmholtz free energy $\psi$ can be additively split into the elastic part $\psi_\mathrm{e}$ and transformation part $\psi_\mathrm{t}$, where the elastic part depends on elastic strain $\boldsymbol{E}_\mathrm{e}$, while the transformation part depends only on transformation strains $\boldsymbol{E}_\mathrm{t}$:

$$\psi(\boldsymbol{E}_\mathrm{e}, \boldsymbol{E}_\mathrm{t}) = \psi_\mathrm{e}(\boldsymbol{E}_\mathrm{e}) + \psi_\mathrm{t}(\boldsymbol{E}_\mathrm{t}), \tag{2}$$

where $\psi_\mathrm{e}$ is St. Venant-Kirchhoff strain–energy function is defined as:

$$\psi_\mathrm{e}(\boldsymbol{E}_\mathrm{e}) = \frac{\lambda}{2}\left(\mathrm{tr}(\boldsymbol{E}_\mathrm{e})\right)^2 + \mu\,\mathrm{tr}\left((\boldsymbol{E}_\mathrm{e})^2\right), \tag{3}$$

where $\mu$ and $\lambda$ are Lamé coefficients. According to [37,43] transformation part $\psi_\mathrm{t}$ is defined as:

$$\begin{aligned}\psi_\mathrm{t}(E_\mathrm{t}^*) = {} & \frac{h_0}{2}\left(E_\mathrm{t}^*\right)^2 + (h_1 - h_0)\left[\frac{1}{2}\left(E_\mathrm{t}^*\right)^2 - \frac{1}{b}\left(E_\mathrm{t}^* - \frac{1}{b}\left(1 - e^{-b\,E_\mathrm{t}^*}\right)\right)\right] + \\ & + \frac{2\,h_3}{\pi}\left(E_t^*\arctan(c\varepsilon_3) + (E_\mathrm{t}^* - \varepsilon_3)\arctan\left(c\,E_\mathrm{t}^* - c\,\varepsilon_3\right) - \right. \\ & \left. - \frac{1}{2\,c}\ln\left(c^2\,\varepsilon_3^2 - 2\,\varepsilon_3\,c^2\,E_\mathrm{t}^* + c^2\,(E_\mathrm{t}^*)^2 + 1\right)\right) + \\ & + (h_2 - h_1)\begin{cases} 0, & 0 \le E_\mathrm{t}^* \le \varepsilon_1, \\ (\varepsilon_2 - \varepsilon_1)\left(\frac{\xi^5}{2} - \frac{\xi^6}{2} + \frac{\xi^7}{7}\right), & \varepsilon_1 \le E_\mathrm{t}^* \le \varepsilon_2, \\ \frac{1}{7}(\varepsilon_2 - \varepsilon_1) + \frac{1}{2}(\varepsilon_2 - \varepsilon_1)(E_\mathrm{t}^* - \varepsilon_2) & \\ \quad + \frac{1}{2}(E_\mathrm{t}^* - \varepsilon_2)^2, & \varepsilon_2 \le E_\mathrm{t}^*, \end{cases}\end{aligned} \tag{4}$$

where $\xi = (E_\mathrm{t}^* - \varepsilon_1)/(\varepsilon_2 - \varepsilon_1)$ and $h_0$, $h_1$, $h_2$, $h_3$, $b$, $c$, $\varepsilon_1$, $\varepsilon_2$, and $\varepsilon_3$ are material parameters. Parameters $h_0$ and $b$ determine the stress value at which transformation starts, while $h_1$ represents the slope of the curve in stress–strain diagram during the transformation and $\varepsilon_1$ determines at which strain the transformation is approximately finished and the slope of curve in stress–strain diagram starts to increase. On the other hand, parameters $h_2$ and $\varepsilon_2$ determine the behavior of the material after the transformation is finished, while parameters $c$, $h_3$, and $\varepsilon_3$ define the behavior of the material during plastic deformations. Equivalent transformation strain $E_\mathrm{t}^*$ is defined as:

$$E_\mathrm{t}^* = J_2\, f(J_\mathrm{r}), \tag{5}$$

with

$$f(J_\mathrm{r}) = \cos\left(\frac{1}{3}\arccos\left(1 - a\,(J_\mathrm{r}^3 + 1)\right)\right) \quad \text{and} \quad J_\mathrm{r} = \frac{J_3}{J_2}, \tag{6}$$

where deviatoric strain invariants $J_2$ and $J_3$ are defined as:

$$J_2 = \left(\frac{2}{3}\,\mathrm{tr}\left(\left(\boldsymbol{E}_\mathrm{t}^\mathrm{D}\right)^2\right)\right)^{1/2} \text{and} \quad J_3 = \left(\frac{4}{3}\,\mathrm{tr}\left(\left(\boldsymbol{E}_\mathrm{t}^\mathrm{D}\right)^3\right)\right)^{1/3}. \tag{7}$$

Here, the deviatoric part of $\boldsymbol{E}_\mathrm{t}$ is defined as: $\boldsymbol{E}_\mathrm{t}^\mathrm{D} = \boldsymbol{E}_\mathrm{t} - 1/3\,\mathrm{tr}(\boldsymbol{E}_\mathrm{t})\,\mathbf{1}$. In Eq. (6) material parameter $a \in [0, 1)$ accounts for compression–tension asymmetry. For $a = 0$ asymmetry is neglected, while $a > 0$ asymmetry is taken into account.

The Clausius-Duhem inequality of the second law of thermodynamics states the following:

$$\mathscr{D} = \boldsymbol{\sigma} : \dot{\boldsymbol{E}} - \dot{\psi} \ge 0, \tag{8}$$

where $\boldsymbol{\sigma}$ is the stress tensor. Inserting Eq. (2) into Eq. (8) yields:

$$\underbrace{\left(\boldsymbol{\sigma} : \dot{\boldsymbol{E}} - \frac{\partial \psi_\mathrm{e}}{\partial \boldsymbol{E}_\mathrm{e}} : \dot{\boldsymbol{E}}\right)}_{①} + \frac{\partial \psi_\mathrm{e}}{\partial \boldsymbol{E}_\mathrm{e}} : \dot{\boldsymbol{E}}_\mathrm{t} - \frac{\partial \psi_\mathrm{t}}{\partial \boldsymbol{E}_\mathrm{t}} : \dot{\boldsymbol{E}}_\mathrm{t} \ge 0. \tag{9}$$

In case of elastic response, where $\mathscr{D} = 0$, expression ①in Eq. (9) yields $\boldsymbol{\sigma} = \partial\psi_\mathrm{e}/\partial\boldsymbol{E}_\mathrm{e}$. Using this relation the inelastic dissipation for the case of transformation can be expressed as:

$$\mathscr{D}_\mathrm{t} = (\boldsymbol{\sigma} - \boldsymbol{\alpha}) : \dot{\boldsymbol{E}}_\mathrm{t} \ge 0, \tag{10}$$

where back-stress tensor $\boldsymbol{\alpha}$ is defined as:

$$\boldsymbol{\alpha} = \frac{\partial \psi_\mathrm{t}}{\partial \boldsymbol{E}_\mathrm{t}} = \underbrace{\frac{\partial \psi_\mathrm{t}}{\partial E_\mathrm{t}^*}}_{\boxed{1}}\,\underbrace{\frac{\partial E_\mathrm{t}^*}{\partial \boldsymbol{E}_\mathrm{t}}}_{\boxed{2}}. \tag{11}$$

Partial differential labeled as $\boxed{1}$ can be expressed as:

$$\begin{aligned}\frac{\partial \psi_\mathrm{t}}{\partial E_\mathrm{t}^*} = {} & h_0\,E_\mathrm{t}^* + (h_1 - h_0)\left[E_\mathrm{t}^* - \frac{1}{b}\left(1 - e^{-b\,E_\mathrm{t}^*}\right)\right] + \\ & + \frac{2\,h_3}{\pi}\left(\arctan\left(c\,\varepsilon_3\right) + \arctan\left(c\,E_\mathrm{t}^* - c\,\varepsilon_3\right)\right) + \\ & + (h_2 - h_1)\begin{cases} 0, & 0 \le E_\mathrm{t}^* \le \varepsilon_1, \\ (\varepsilon_2 - \varepsilon_1)(2.5\,\xi^4 - 3\,\xi^5 + \xi^6), & \varepsilon_1 \le E_\mathrm{t}^* \le \varepsilon_2, \\ 0.5\,(\varepsilon_2 - \varepsilon_1) + (E_\mathrm{t}^* - \varepsilon_2), & \varepsilon_2 \le E_\mathrm{t}^*, \end{cases}\end{aligned} \tag{12}$$

while partial derivative labeled as $\boxed{2}$ yields to:

$$\frac{\partial E_\mathrm{t}^*}{\partial \boldsymbol{E}_\mathrm{t}} = \left(f(J_\mathrm{r}) - J_\mathrm{r}\,f'\right)\frac{2}{3\,J_2}\,\boldsymbol{E}_\mathrm{t}^\mathrm{D} + \frac{4}{3\,J_3^2}\left[\left(\boldsymbol{E}_\mathrm{t}^\mathrm{D}\right)^2 - \frac{J_2^2}{2}\,\mathbf{1}\right]. \tag{13}$$

By defining a tensor $\boldsymbol{B} = \boldsymbol{\sigma} - \boldsymbol{\alpha}$ and taking into account its symmetry, the transformation function $f(\boldsymbol{B})$ is defined as [43]:

$$f(\boldsymbol{B}) = \sqrt{\frac{3}{2}}\left\|\boldsymbol{B}^\mathrm{D}\right\| - \sigma_0, \tag{14}$$

where $\sigma_0$ is the material parameter that defines the radius of the elastic domain.

Among all the admissible states of transformation (according to inequality in Eq. (8)) we choose the stress state that yields the maximum dissipation $\mathscr{D}_\mathrm{t}$ or the minimum of $-\mathscr{D}_\mathrm{t}$. The original problem can be recast into the unconstrained minimization problem by using the method of Lagrangian multipliers with the Lagrangian function defined as:

$$\mathscr{L}(\boldsymbol{B}, \dot{\gamma}) = -\mathscr{D}_\mathrm{t}(\boldsymbol{B}) + \dot{\gamma}\,f(\boldsymbol{B}), \tag{15}$$

where $\gamma$ is a Lagrangian multiplier. Minimum of $\mathscr{L}(\boldsymbol{B},\dot{\gamma})$ must satisfy Karush-Kuhn–Tucker conditions:

$$\frac{\partial \mathscr{L}(\boldsymbol{B},\dot{\gamma})}{\partial \boldsymbol{B}} = 0, \quad f(\boldsymbol{B}) \le 0, \quad \dot{\gamma} \ge 0, \quad \dot{\gamma}\, f(\boldsymbol{B}) = 0, \tag{16}$$

and from Eq. $(16)_1$ the evolution equation for the internal variable of the material model can be derived:

$$\dot{\boldsymbol{E}}_{\mathrm{t}} = \dot{\gamma}\, \frac{\partial f(\boldsymbol{B})}{\partial \boldsymbol{B}} = \sqrt{6}\,\dot{\gamma}\, \frac{\boldsymbol{B}^{\mathrm{D}}}{\left\| \boldsymbol{B}^{\mathrm{D}} \right\|}. \tag{17}$$

With that, all constitutive equations are defined. For details on numerical implementation see [42].

### 2.2. 7-Parameter shell element

Within this section, a concise overview of a 7-parameter finite-rotation-shell model is provided. For a more comprehensive derivation, cf. [42,45–48]. The derivation of shell kinematics assumes a quadratic through-the-thickness variation of displacements and employs an extensible-director kinematic hypothesis. Standard notation for the indices is adopted as follows: small Latin letters for indices $1,2,3$ and small Greek letters for indices 1,2.

The shell is embedded in 3D space with a fixed orthonormal basis $\{e_i\}$. It is characterized as a surface with an extensible director field, while the position vector to the material point in the initial configuration is defined as:

$$\begin{aligned} &\boldsymbol{X}\left(\xi^1,\xi^2,\xi^3\right) = \boldsymbol{\varphi}_0\left(\xi^1,\xi^2\right) + \xi^3\, \boldsymbol{D}\left(\xi^1,\xi^2\right), \\ &\xi^3 \in \left[-h/2, h/2\right], \quad \left(\xi^1,\xi^2\right) \in \mathcal{A}, \quad \|\boldsymbol{D}\| = 1, \end{aligned} \tag{18}$$

where $\xi^i$ are the convected curvilinear coordinates. The vector $\boldsymbol{\varphi}_0$ represents the mid-surface $\mathscr{M}$ of the shell, while $\boldsymbol{D}$ is a unit-length vector field normal-to-the-$\mathscr{M}$, known as the shell director. Furthermore, $h$ defines the initial thickness of the shell, and $\mathcal{A}$ denotes the domain for the mid-surface parameterization. Henceforth, the writing of functions' and functionals' arguments will be omitted for brevity. The position vector to the material point in the deformed (current) configuration is assumed to be:

$$\boldsymbol{x} = \underbrace{\boldsymbol{\varphi}_0 + \boldsymbol{u}}_{\boldsymbol{\varphi}} + \xi^3 \underbrace{\overline{\lambda}\,\boldsymbol{a}}_{\boldsymbol{d}} + \left(\xi^3\right)^2 \underbrace{q\,\boldsymbol{a}}_{\boldsymbol{f}}, \quad \|\boldsymbol{a}\| = 1, \tag{19}$$

where $\boldsymbol{u}$ is the displacement vector field at the mid-surface, $\overline{\lambda}$ is a through-the-thickness-stretching scalar field, and $q$ is a hierarchical scalar field associated with the quadratic variation of displacements in the through-the-thickness direction. Additionally, $\boldsymbol{a}$ denotes the rotated shell director field in the deformed configuration (see [49–51] for details). Using Eqs. (18) and (19), the covariant base vectors for both the initial and deformed configurations are

$$\begin{aligned} \boldsymbol{G}_\alpha &= \frac{\partial \boldsymbol{X}}{\partial \xi^\alpha} = \boldsymbol{\varphi}_{0,\alpha} + \xi^3\, \boldsymbol{D}_{,\alpha}, \quad \boldsymbol{G}_3 = \frac{\partial \boldsymbol{X}}{\partial \xi^3} = \boldsymbol{D}, \\ \boldsymbol{g}_\alpha &= \frac{\partial \boldsymbol{x}}{\partial \xi^\alpha} = \boldsymbol{\varphi}_{,\alpha} + \xi^3\, \boldsymbol{d}_{,\alpha} + \left(\xi^3\right)^2 \boldsymbol{f}_{,\alpha}, \quad \boldsymbol{g}_3 = \frac{\partial \boldsymbol{x}}{\partial \xi^3} = \boldsymbol{d} + 2\,\xi^3\, \boldsymbol{f}, \end{aligned} \tag{20}$$

where $\boldsymbol{d}_{,\alpha} = \overline{\lambda}_{,\alpha}\,\boldsymbol{a} + \overline{\lambda}\,\boldsymbol{a}_{,\alpha}$ and $\boldsymbol{f}_{,\alpha} = q_{,\alpha}\,\boldsymbol{a} + q\,\boldsymbol{a}_{,\alpha}$. The dual base vectors $\boldsymbol{G}^i$ are defined through the orthogonal condition $\boldsymbol{G}^i \cdot \boldsymbol{G}_j = \delta^i_j$, where $\delta^i_j$ is the Kronecker delta symbol. For the considered shell model the Green–Lagrange strain tensor is defined as:

$$\check{\boldsymbol{E}} = \frac{1}{2}\left(\boldsymbol{g}_i \cdot \boldsymbol{g}_j - \boldsymbol{G}_i \cdot \boldsymbol{G}_j\right) \boldsymbol{G}^i \otimes \boldsymbol{G}^j = \check{E}_{ij}\, \boldsymbol{G}^i \otimes \boldsymbol{G}^j\,, \tag{21}$$

where the covariant components of the strain tensor are expressed as functions of the coordinate $\xi^3$, as detailed in [47]:

$$\check{E}_{ij} = H_{ij} + \xi^3\, K_{ij} + \left(\xi^3\right)^2 L_{ij} + \left(\xi^3\right)^3 M_{ij} + \left(\xi^3\right)^4 N_{ij}. \tag{22}$$

Following [47], the Eq. (22) undergoes truncation after the quadratic term, resulting in a reduced form:

$$\check{E}_{ij} \to E_{ij} = H_{ij} + \xi^3\, K_{ij} + \left(\xi^3\right)^2 L_{ij}. \tag{23}$$

The explicit forms of the covariant components of the reduced strain tensor $\boldsymbol{E} = E_{ij}\, \boldsymbol{G}^i \otimes \boldsymbol{G}^j$ are:

$$\begin{aligned} H_{\alpha\beta} &= \frac{1}{2}\left(\boldsymbol{\varphi}_{,\alpha} \cdot \boldsymbol{\varphi}_{,\beta} - \boldsymbol{\varphi}_{0,\alpha} \cdot \boldsymbol{\varphi}_{0,\beta}\right), \quad H_{\alpha 3} = \frac{1}{2}(\boldsymbol{\varphi}_{,\alpha} \cdot \mathbf{d} - \underbrace{\boldsymbol{\varphi}_{0,\alpha} \cdot \boldsymbol{D}}_{0}), \\ H_{33} &= \frac{1}{2}(\boldsymbol{d} \cdot \boldsymbol{d} - \boldsymbol{D} \cdot \boldsymbol{D}) = \frac{1}{2}\left(\overline{\lambda}^2 - 1\right), \end{aligned} \tag{24}$$

$$\begin{aligned} K_{\alpha\beta} &= \frac{1}{2}\left(\boldsymbol{\varphi}_{,\alpha} \cdot \boldsymbol{d}_{,\beta} + \boldsymbol{\varphi}_{,\beta} \cdot \boldsymbol{d}_{,\alpha} - \boldsymbol{\varphi}_{0,\alpha} \cdot \boldsymbol{D}_{,\beta} - \boldsymbol{\varphi}_{0,\beta} \cdot \boldsymbol{D}_{,\alpha}\right), \\ K_{\alpha 3} &= \frac{1}{2}\left(\boldsymbol{d}_{,\alpha} \cdot \boldsymbol{d} + 2\,\boldsymbol{\varphi}_{,\alpha} \cdot \boldsymbol{f} - \underbrace{\boldsymbol{D}_{,\alpha} \cdot \boldsymbol{D}}_{0}\right), \quad K_{33} = \frac{1}{2}\left(4\,\boldsymbol{f} \cdot \boldsymbol{d}\right) = 2\,\boldsymbol{f} \cdot \boldsymbol{d} = 2\,q\,\overline{\lambda}, \end{aligned} \tag{25}$$

$$\begin{aligned} L_{\alpha\beta} &= \frac{1}{2}\left(\boldsymbol{d}_{,\alpha} \cdot \boldsymbol{d}_{,\beta} + \boldsymbol{\varphi}_{,\alpha} \cdot \boldsymbol{f}_{,\beta} + \boldsymbol{\varphi}_{,\beta} \cdot \boldsymbol{f}_{,\alpha} - \boldsymbol{D}_{,\alpha} \cdot \boldsymbol{D}_{,\beta}\right), \\ L_{\alpha 3} &= \frac{1}{2}\left(2\boldsymbol{d}_{,\alpha} \cdot \boldsymbol{f} + \boldsymbol{f}_{,\alpha} \cdot \boldsymbol{d}\right), \quad L_{33} = \frac{1}{2}\left(4\boldsymbol{f} \cdot \boldsymbol{f}\right) = 2\,\boldsymbol{f} \cdot \boldsymbol{f} = 2\,q^2. \end{aligned} \tag{26}$$

Note that in the computer code, the covariant components are defined by Eqs. (24)–(26) undergo transformation into Cartesian components, using the local Cartesian basis defined for each integration point.

The weak form of the equilibrium equations at time $t_{n+1}$ is (index $n+1$ is omitted hereinafter for brevity):

$$G\left(\boldsymbol{\Phi}, \boldsymbol{E}_{\mathrm{t}}, \delta\boldsymbol{\Phi}\right) = \int_{\mathscr{M}} \int_{-h/2}^{h/2} \delta\boldsymbol{E}\left(\boldsymbol{\Phi}, \delta\boldsymbol{\Phi}\right) : \boldsymbol{\sigma}\left(\boldsymbol{E}\left(\boldsymbol{\Phi}\right), \boldsymbol{E}_{\mathrm{t}}\right) \mathrm{d}V - G_{\mathrm{ext}}\left(\delta\boldsymbol{\Phi}\right) = 0, \tag{27}$$

where $\boldsymbol{\Phi} = \{\boldsymbol{u}, \boldsymbol{a}, \overline{\lambda}, q\}$ is a set of unknown functions called generalized displacements, $\delta\boldsymbol{\Phi} = \left[\delta\boldsymbol{u}, \delta\boldsymbol{a}, \delta\overline{\lambda}, \delta q\right]^{\mathrm{T}}$ is the vector of admissible variations of $\boldsymbol{\Phi}$, $\delta\boldsymbol{E} = \partial\boldsymbol{E}/\partial\boldsymbol{\Phi} \cdot \delta\boldsymbol{\Phi} = \frac{\mathrm{d}}{\mathrm{d}\epsilon}[\boldsymbol{E}\left(\boldsymbol{\Phi} + \epsilon\,\delta\boldsymbol{\Phi}\right)]_{\epsilon=0}$ is the variation of the reduced strain tensor.

Once the mid-surface $\mathscr{M}$ is spatially discretized using $n_{\mathrm{el}}$ non-overlapping finite elements (where $\mathscr{M} \approx \bigcup_{e=1}^{n_{\mathrm{el}}} A_e$), and appropriate interpolation methods are applied for generalized displacements and their admissible variations, functional in Eq. (27) transforms into an assembly of the finite-element contributions. This assembly involves mesh-related nodal values for generalized displacements and unknowns in the form of Gauss-point-related values for the transformation tensor $\boldsymbol{E}_{\mathrm{t}}$:

$$G = \mathbb{A}_{e=1}^{n_{\mathrm{el}}} \left( \underbrace{G^e_{\mathrm{int}}\left(\boldsymbol{\Phi}^e, \boldsymbol{E}_{\mathrm{t}}, \delta\boldsymbol{\Phi}^e\right) - G^e_{\mathrm{ext}}\left(\delta\boldsymbol{\Phi}^e\right)}_{=0} \right) = 0. \tag{28}$$

Here, $\mathbb{A}$ denotes the finite-element-assembly operator (see [52] for details), and $G^e_{\mathrm{int}}$ and $G^e_{\mathrm{ext}}$ denote the element's approximation of the first and second terms on the right-hand side of Eq. (27), respectively:

$$G^e = \int_{A_e} \int_{-h/2}^{h/2} \delta\boldsymbol{E}\left(\boldsymbol{\Phi}^e, \delta\boldsymbol{\Phi}^e\right) : \boldsymbol{\sigma}\left(\boldsymbol{E}\left(\boldsymbol{\Phi}^e\right), \boldsymbol{E}_{\mathrm{t}}\right) \mathrm{d}V - G^e_{\mathrm{ext}}\left(\delta\boldsymbol{\Phi}^e\right) = 0. \tag{29}$$

The current values of the stress tensor $\boldsymbol{\sigma}$ are obtained by evaluating a trial step in which elastic response is assumed. This is the first step of the two for the operator-split method. In the second step, where the solution $\mathbb{A}_{e=1}^{n_{\mathrm{el}}} \boldsymbol{\Phi}^e$ is computed for a given loading, the linearization of Eq. (29) is needed, which can be written as $\mathrm{Lin}\left(G^e\right) = G^e + \Delta G^e$, where

$$\Delta G^e = \int_{A_e} \int_{-h/2}^{h/2} (\delta\boldsymbol{E} : \mathbb{C}\, \Delta\boldsymbol{E} + \Delta(\delta\boldsymbol{E}) : \boldsymbol{\sigma})\, \mathrm{d}V. \tag{30}$$

Here, $\mathbb{C} = \partial\boldsymbol{S}/\partial\boldsymbol{E}$ is the fourth-order tensor, called the consistent inelastic tangent operator, which is computed already in the first step, and

$$\Delta\boldsymbol{E} = \frac{\partial\boldsymbol{E}}{\partial\boldsymbol{\Phi}^e} \cdot \Delta\boldsymbol{\Phi}^e, \quad \delta\boldsymbol{E} = \frac{\partial\boldsymbol{E}}{\partial\boldsymbol{\Phi}^e} \cdot \delta\boldsymbol{\Phi}^e, \quad \Delta(\delta\boldsymbol{E}) = \frac{\partial(\delta\boldsymbol{E})}{\partial\boldsymbol{\Phi}^e} \cdot \Delta\boldsymbol{\Phi}^e. \tag{31}$$

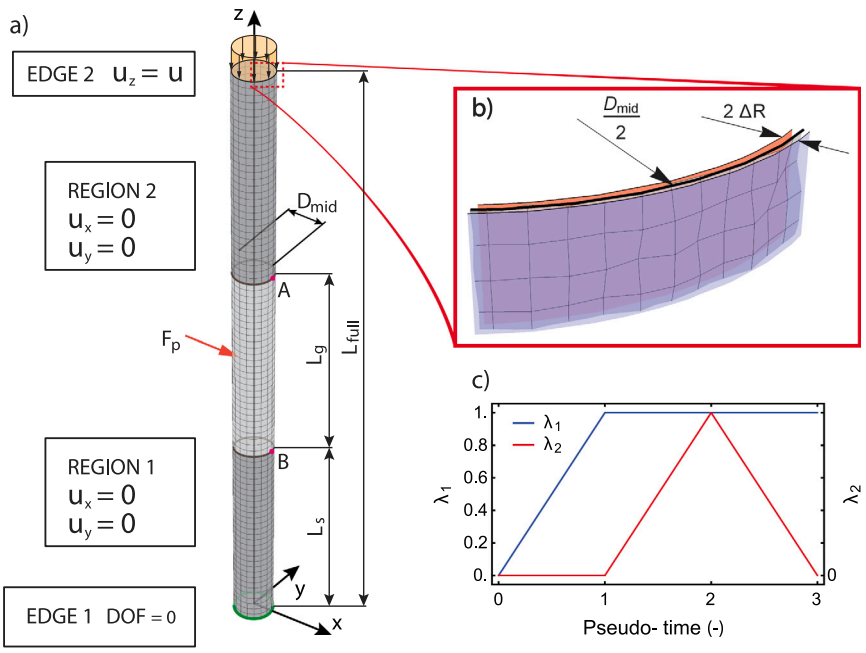


**Fig. 1.** Tube in compression: (a) geometry, mesh, boundary, and loading conditions, (b) detailed view of random perturbation of structural mesh in radial direction, and (c) change of loading multipliers.

For details on finite element formulations of the 7-parameter shell model, the reader is referred to [42].

## 3. Numerical simulations

Numerical treatment of the shell model and SMA constitutive equations was performed in *Mathematica* using finite element code generator AceGen [53,54] to obtain and manipulate numerical expressions. Next, AceFEM package [55] was used to define and solve the boundary problem presented in the next section.

### 3.1. The boundary problem

We considered a tube of full length $L_{\text{full}}$, gauge length $L_{\text{g}}$, middle diameter $D_{\text{mid}}$ (as shown in Fig. 1), and thickness $h$ in order to simulate an isothermal loading as in the experiments, where tubes of different dimensions were tested [40].

The tube is fully clamped at the bottom edge (all degrees of freedom are set to 0), while in regions $z \in [0,\ L_{\text{s}}]$ and $z \in [L_{\text{full}} - L_{\text{s}},\ L_{\text{full}}]$ the allowed displacement of nodes is limited to $z$-direction, the same as in the experiments [40]. Similarly, the length of the supported part of the tube $L_{\text{s}} = 10.5$ mm is also identical to the ones in the experiments.

Based on the preliminary simulations, the use of 72 finite elements in the circumferential direction is sufficient and a converged solution is obtained (practically no difference is observed in the response of the tube compared to the results obtained with 96 finite elements in the circumferential direction). The number of elements in the axial direction is defined by equations:

$$N_{\text{z1}} = \text{rounded}\left[\frac{N_\phi\, L_{\text{g}}}{\pi\, D_{\text{mid}}}\right], \tag{32}$$

$$N_{\text{z2}} = \text{rounded}\left[\frac{N_\phi\, L_{\text{s}}}{\pi\, D_{\text{mid}}}\right], \tag{33}$$

where $N_{z1}$ and $N_{z2}$ are the numbers of elements in the axial direction at the gauge part of the tube and at the supported part of the tube, respectively, and $N_\phi$ is a number of elements in the circumferential direction. By defining the number of elements in this way, the best-structured mesh is obtained, i.e., elements are almost square-shaped. Note that the mesh shown in Fig. 1(a) is coarser for the sake of visibility.

In order to induce buckling of the tube in the simulation (in which the geometry is usually defined as perfect) an imperfection must be introduced. Various approaches have been used in the literature to assign the imperfection, e.g., geometric imperfection in the form of axisymmetric and non-axisymmetric waves at the end of the tube [36,37], asymmetric geometric imperfection in the middle of the tube [38], or geometric imperfection as artificial random defects of the initial geometry [34]. Although oriented geometric imperfections (such as axisymmetric and non-axisymmetric waves or eigenmodes) allow straightforward reproduction of buckling modes in such a way that the response of the tubes is comparable to the experiments, their main drawback is the prejudgment of the buckling mode. Moreover, different assigned waves and their combinations lead to different buckling modes. For simulations that aim to predict the buckling response of the tubes (without being experimentally characterized), the use of this form of imperfection is inappropriate due to unknown factors, e.g., which waves to assign, what is the amplitude for each wave, etc. Therefore, the use of a random, non-biased imperfection suitable to obtain accurate results for thick/thin and short/long tubes that exhibit different buckling modes is required.

We considered a combination of two types of imperfections: (*i*) random perturbation of structural mesh in the radial direction and (*ii*) lateral perturbation force. As explained in Appendix A, the combination of these two imperfections produces the most comparable results with respect to experimental observations. To the best of our knowledge, this combination has not been previously used. The primary advantage of this approach lies in its minimal impact on the exhibited buckling modes, which in most simulations closely matches the observations from the experiments. This eliminates the need of guessing/imposing the eigenmodes beforehand, as is often done when using eigenmodes as the initial geometric imperfection. The maximal amplitude of mesh perturbation is $\Delta R = A_{\text{m}}\, h$, where $A_{\text{m}}$ is the maximal relative amplitude of mesh perturbation and $h$ is the wall thickness of the tube. The actual value of mesh perturbation in the radial direction for each node is determined with uniform probability distribution in the range from $-\Delta R$ to $+\Delta R$ (see Fig. 1(b)) with a standard deviation of $\Delta R/\sqrt{3}$. The

**Table 1**
Middle diameter $D_{mid}$ and wall thickness $h$ of the tubes considered in the numerical simulations with corresponding maximal applied axial force $F_{max}$ and labels. Symbol * by the labels notes that the tube was also tested experimentally in [40]. The number after the letter D represents the outer diameter of the tube, while the number after Dt represents the diameter-to-thickness ratio.

| Tube label | $D_{mid}$ (mm) | $h$ (mm) | $F_{max}$ (N) |
|---|---|---|---|
| D2&Dt5 | 1.6 | 0.4 | 2312 |
| D2&Dt10 | 1.8 | 0.2 | 1301 |
| *D2&Dt12 | 1.835 | 0.165 | 1094 |
| D2&Dt13 | 1.85 | 0.15 | 1003 |
| D2&Dt15 | 1.865 | 0.135 | 910 |
| D2&Dt16 | 1.87 | 0.13 | 863 |
| D2&Dt17 | 1.88 | 0.12 | 815 |
| D2&Dt25 | 1.92 | 0.08 | 555 |
| *D2.5&Dt5 | 2 | 0.5 | 3613 |
| *D2.5&Dt10 | 2.25 | 0.25 | 2032 |
| *D2.5&Dt12 | 2.29 | 0.21 | 1737 |
| D2.5&Dt13 | 2.31 | 0.19 | 1586 |
| D2.5&Dt15 | 2.33 | 0.17 | 1431 |
| D2.5&Dt16 | 2.34 | 0.16 | 1353 |
| *D2.5&Dt17 | 2.35 | 0.15 | 1274 |
| *D2.5&Dt25 | 2.4 | 0.1 | 867 |
| D3&Dt5 | 2.4 | 0.6 | 5202 |
| D3&Dt10 | 2.7 | 0.3 | 2926 |
| *D3&Dt12 | 2.75 | 0.25 | 2484 |
| D3&Dt13 | 2.77 | 0.23 | 2279 |
| D3&Dt15 | 2.80 | 0.21 | 2070 |
| D3&Dt16 | 2.81 | 0.19 | 1953 |
| D3&Dt17 | 2.82 | 0.18 | 1834 |
| D3&Dt25 | 2.88 | 0.12 | 1249 |

amplitude of force perturbation is $F_p = F_{max} A_f$, where $A_f$ is the relative force amplitude and $F_{max}$ is the value of axial force that yields axial stress $\sigma_{max} = 1150$ MPa (see Table 1), which in the evaluated tubes corresponds well above the end of the transformation plateau (see Fig. 2), where eCE is maximized.

Perturbation force is applied at the middle of the tube in the node with coordinates $(-D_{mid}/2, 0, L_{full}/2)$ and is oriented in the direction of positive $x$-axis (see Fig. 1(a)). It is applied as $F_1 = F_p \lambda_1$, where $\lambda_1$ is a load multiplier. Compression loading is applied at the top edge in the form of displacement $u_2 = u \lambda_2$, where $u$ is a displacement in $-z$ direction and $\lambda_2$ is a load multiplier. Loading procedure consists of three steps as shown in Fig. 1(c): $(i)$ increase of $\lambda_1$ from 0 to 1 at constant $\lambda_2 = 0$, $(ii)$ increase of $\lambda_2$ from 0 until one of the two limits (defined in the following sentence) are reached at constant $\lambda_1 = 1$, and $(iii)$ decrease of $\lambda_2$ back to 0 at constant $\lambda_1 = 1$. In the second step $(ii)$ of the procedure two different limits are considered, namely, stress limit $\sigma = F/A \geq \sigma_{max}$, where $F$ is a reaction force in the $z$-direction at the bottom edge of the tube and $A$ is the initial cross-section of the tube, and strain limit $\varepsilon = \Delta L/L_g \geq \varepsilon_{lim}$, where $\Delta L$ is a relative displacement of node A with coordinates $(D_{mid}/2, 0, L_s+L_g)$ with respect to the node B with coordinates $(D_{mid}/2, 0, L_s)$, see Fig. 1(a). The value of maximal stress $\sigma_{max}$ is set to 1150 MPa (corresponding $F_{max}$ is given in Table 1) and strain limit $\varepsilon_{lim}$ is set to 6 % for tubes without failure, while lower strain limit values are used for tubes that failed. In several cases, the lower value of the strain limit matches the maximal measured strain in the experiment, while in other cases, the strain limit is defined in such a way that the tubes are able to fully exhibit their buckling mode. It has to be noted, that the value of displacement $u$ is not important as long as it is large enough so that one of two limits is reached in the second step of the loading procedure. Also, it should be noted that the arc-length method was used to obtain a converged solution.

Material parameters used in our simulations are gathered in Table 2, while the details on material parameter identification are presented in the following section.

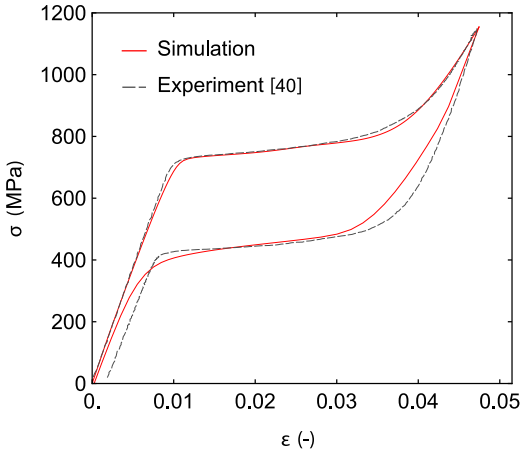


**Fig. 2.** Comparison of experimental and numerical response in stress–strain diagram of D2.5&Dt12 tube with gauge length of $L_g = 10$ mm.

### 3.2. Material parameter identification

Material parameters were used based on the experimental measurements [40] of the D2.5&Dt12 tube with $L_g = 10$ mm that exhibited the least unstable response, i.e., the least visible buckling–unbuckling (BUB), when subjected to an isothermal compression loading. The boundary problem presented in the previous section was considered in numerical simulation, while imperfections with amplitudes $A_f = 0.1$ % and $A_m = 3$ % were used since they fitted the experimental results most accurately as presented in Appendix A. Note that material parameters obtained considering the tube without imperfections resulted in a poor match between experimental and numerically results. As already mentioned above, the tube exhibited BUB during the experiments, but the simulations where no imperfections were introduced did not. Material parameters were fitted in such a way that the least square error between the experimental stress–strain curve and simulation was minimized. Table 2 contains identified material parameters that we used in our simulations.

Here, $E$ is the elastic modulus of austenite, $\nu$ is the Poisson ratio, and $\sigma_0$ is the material parameter that defines the radius of the elastic domain. The role of the remaining parameters can be seen from Eq. (4). Note that the material parameter that accounts for compression–tension asymmetry $a$ is taken from [37], while the rest of the material parameters, i.e., $\varepsilon_3$, $h_3$, and $c$, have value 0. Fig. 2 shows a comparison between the numerical and experimental response of the tubes in the stress–strain diagram. Minor discrepancies can be observed between the curves at the end of the unloading, which is due to the neglected irreversible deformation in the material model. This is also the reason for the differences in overall unloading paths between experiment and simulation.

## 4. Results & discussion

### 4.1. Definition of buckling modes

Similar to the experiments in [40] various responses of the tubes were observed in the numerical simulations. In our simulations, we were able to identify several buckling modes and compared them with their experimental counterparts in stress–strain diagrams. The comparison is shown below. Due to the random orientation of displacements during buckling in the experiments (including towards or away from the camera), the experimental buckling modes (displacement fields) are not shown in the comparison with numerical simulations for all tubes. The reader is referred to [40] for more details on the experiments. Identical to [40], a failure of the tube is considered as the loss of the

**Table 2**
Identified material parameters based on experiments [40].

| $E$ (GPa) | $\nu$ | $\sigma_0$ (MPa) | $a$ | $b$ | $h_0$ (GPa) | $h_1$ (GPa) | $h_2$ (GPa) | $\varepsilon_1$ (%) | $\varepsilon_2$ (%) |
|---|---|---|---|---|---|---|---|---|---|
| 78 | 0.3 | 160 | 0.99225 | 2700 | 1570 | 3.37 | $15 \times 10^3$ | 2 | 12.5 |

ability to serve its function, i.e., the inability of the tube to reach the end of the transformation (1150 MPa) due to buckling. Moreover, the critical stress $\sigma_{\text{failure}}$ at which the tube exhibits failure is defined as the maximum stress, after which the curve in the stress–strain diagram starts to decrease drastically (while strain is increasing). Note that in the following figures, only the unclamped part of the tube is shown, i.e., $z \in [L_s, L_s + L_g]$, to increase clarity.

Medium-long and medium-thick tubes, e.g., D2.5&Dt12 with $L_g$ = 14 mm, exhibited global buckling–unbuckling (labeled as GBUB) as shown in Fig. 3, in which the comparison between numerical and experimental responses is shown in a stress–strain diagram. In the case of GBUB, the tube buckles globally (beam-like) at the beginning of the transformation (point 1). During further axial loading, the lateral displacements in the middle of the tube increase (point 2) until the maximum displacements are reached (point 3). Surprisingly, if the tube is stiff enough, an increase in the axial load leads to a straightening of the tube, i.e., to an unbuckling (point 4). The main reason for buckling–unbuckling behavior is that transformation process is not symmetrical around the tube's axis due to imperfections which cause a non-uniform stress distribution. Consequently, transformation on the side where stresses are higher ends before that its counterpart on the opposite side, leading into local stiffening of the tube resulting into straightening of the entire tube. During unloading, the reversed behavior is observed, with the lateral displacements in the middle of the tube first increasing (point 6) and later decreasing (point 7). Although discrepancies between experimental and numerical response are visible in the stress–strain diagram in Fig. 3, the agreement between the curves is acceptable, and, more importantly, their buckling trends match, as GBUB is observed in both cases. Note that the maximum lateral displacements in the simulation are about 0.25 mm in the $x$-direction, while in experiments the lateral displacements were not measured.

Long and thick tubes, e.g., D2.5&Dt5 with $L_g$ = 18 mm, exhibited global buckling (labeled as GB). Fig. 4 shows the comparison between the numerical and experimental response in the stress–strain diagram as well as snapshots of buckling observed experimentally. The tube exhibits global buckling at the beginning of the transformation (point 1), but in contrast to GBUB, the lateral displacements only increase with increasing axial load (points 2 and 3). The stiffness of the tube governs the further development of the buckling. In the simulations, where the tube acts stiffer compared to the experiments, the axial limit force $F_{\max}$ (resulting in axial stress of 1150 MPa) is reached and the unloading starts, whereas in the experiment the tube is softer and the curve (gray dashed line in Fig. 4) is directed downwards after reaching the critical stress $\sigma_{\text{failure}} \approx 1000$ MPa. Note that in the experiments, the start of the unloading of the tube is set manually. Otherwise, the buckling would continue until the tube fracture [40].

Medium-long and medium-thin tubes, e.g., D2.5&Dt17 with $L_g$ = 14 mm, exhibit a global buckling with the transition to a local buckling (labeled as GB+LB1), as shown in Fig. 5. Similar to the previously presented responses, the global buckling occurs at the beginning of the transformation (point 1) and the lateral displacements of the middle part of the tube continue to develop as the axial load increases (point 3). Note that the displacement of the entire cross-section of the tube between point 1 and point 3 is in the $x$-direction. In contrast to GB, where the entire cross-section continues to displace with higher axial loads and remains circular, in the case of GB+LB1, there is a transition to local buckling (point 4), where the cross-section first ovalizes and later the wall of the tube snaps (point 5). Note that in this case, the strain limit $\varepsilon_{\text{lim}} = 0.033$ is reached at point 5, which leads to the

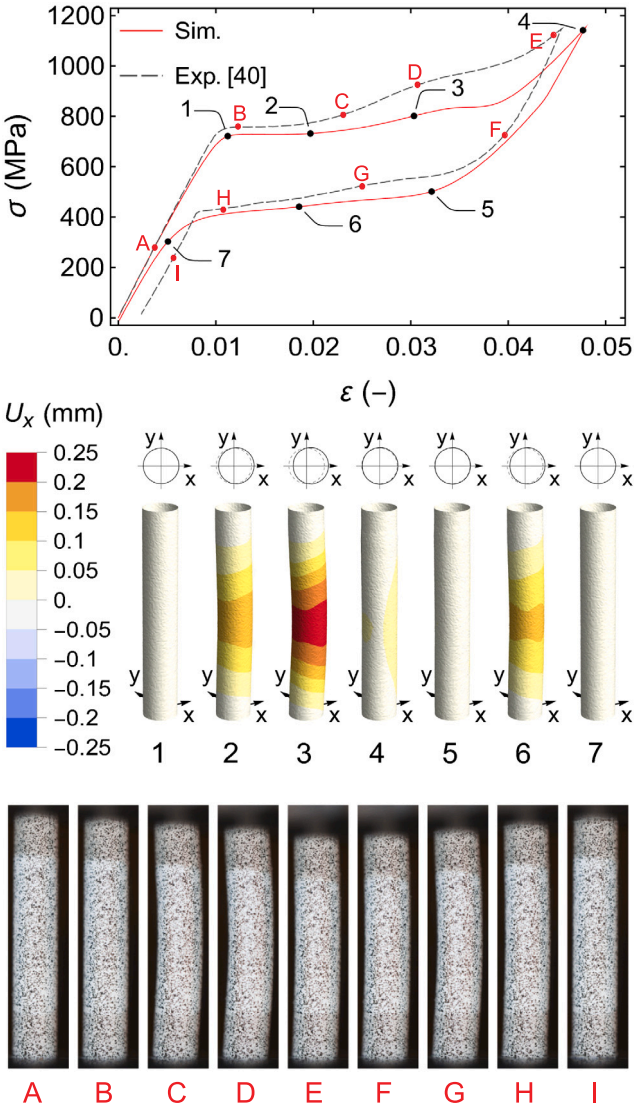


**Fig. 3.** Comparison of the numerical and experimental response in the stress–strain diagram and the buckling modes of D2.5&Dt12 tube with $L_g$ = 14 mm that exhibits global buckling–unbuckling (GBUB).

unloading step. The numerical response in the stress–strain diagram agrees very well with the experimental one. Interestingly, the stress and strain at which failure occurs (point 3) match almost perfectly with the experiments. The main discrepancy in the response after point 3 is in the slope of the curve, which can be attributed to the measuring inaccuracies/errors since the snap-buckling (limit load) phenomena occurs rapidly and the displacements of this section of the tube are out of plane (see [40] for details on measuring accuracy).

In the medium-long and thin tubes, e.g., D2.5&Dt25 with $L_g$ = 14 mm, a local buckling with one wave in the circumferential direction (labeled as LB1) is prevalent. The buckling occurs at the beginning of the transformation (without previous global buckling), as shown in Fig. 6. In this case, only one side of the tube wall displaces with increasing axial load (point 2). At point 4, the strain limit $\varepsilon_{\text{lim}} = 0.016$

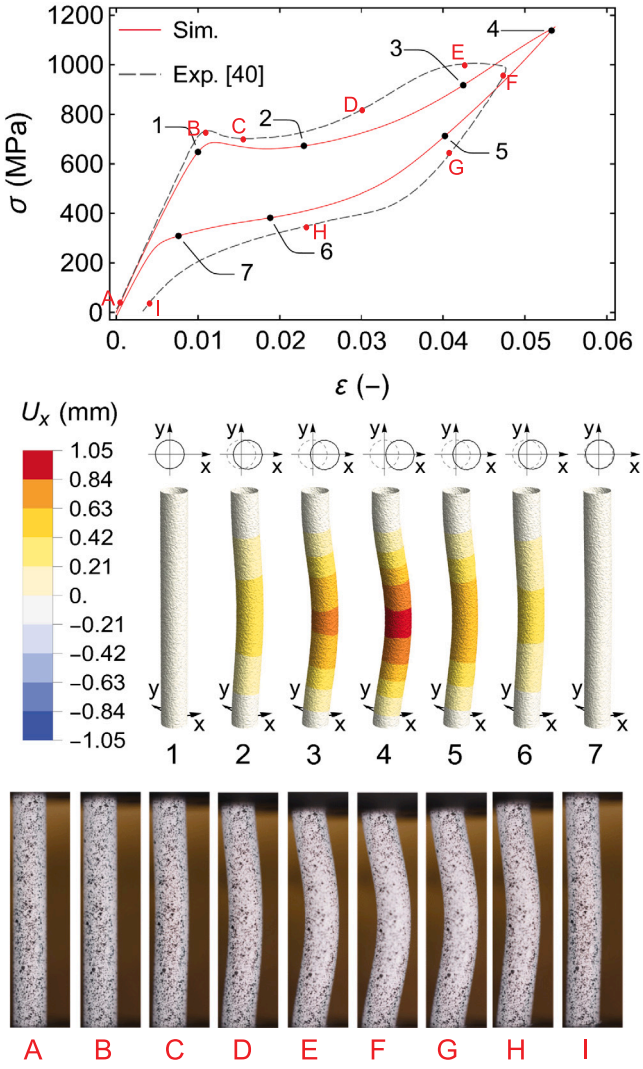


**Fig. 4.** Comparison of the numerical and experimental response in the stress–strain diagram and the buckling modes of D2.5&Dt5 tube with $L_g$ = 18 mm that exhibits global buckling (GB).

is reached, and unloading begins. The general trend of the experimental and numerical response is comparable, while a large discrepancy after the failure can be observed in the stress–strain diagram. We attribute the reason for this to the measurement error after failure (see [40] for details). Nevertheless, the stress and strain values at which the failure occurs in the simulations (point 2) are comparable to those of the experiments. Note that in the simulation unloading starts at lower strain values compared to the experiments due to issues with the convergence of the algorithm at higher strain values.

Short and thin tubes, e.g., D2.5&Dt25 with $L_g$ = 6 mm, exhibited a local buckling with 3 waves in the circumferential direction, as shown in Fig. 7. At the beginning of the transformation (point 1), the instabilities start (they are barely visible in the colored map due to the constant scale for all points) and continue to grow with increasing axial load (point 2) until failure (point 3), from where the stress decreases. Further axial load leads to an increase of the displacements up until the strain limit $\varepsilon_{\text{lim}}$ = 0.036 is reached at point 5. Surprisingly, the stress and strain values of point 5 agree very well with the experimental measurements, although some deviations between the curves can be observed before point 5 is reached. Nevertheless, the general trends of the response of the tubes match well.

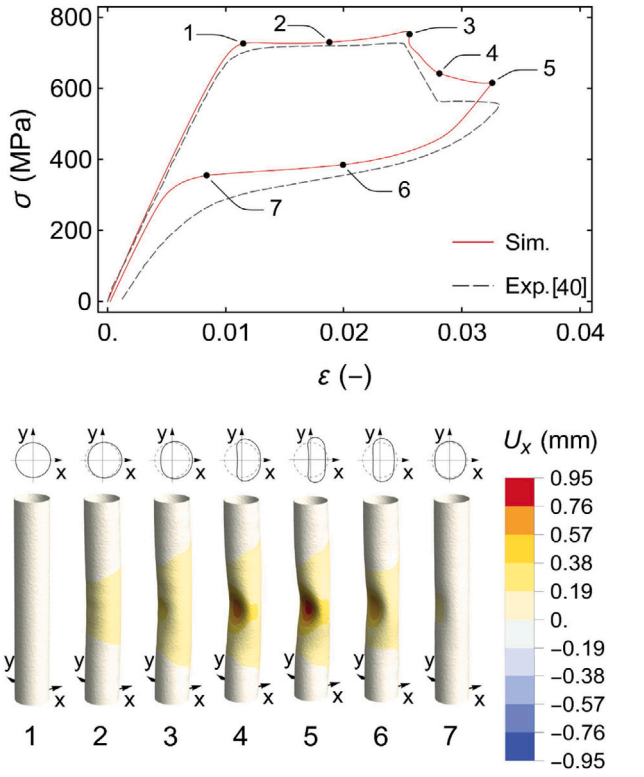


**Fig. 5.** Comparison of the numerical and experimental response in the stress–strain diagram of D2.5&Dt17 tube with $L_g$ = 14 mm that exhibits global buckling with transition to local buckling (GB+LB1).

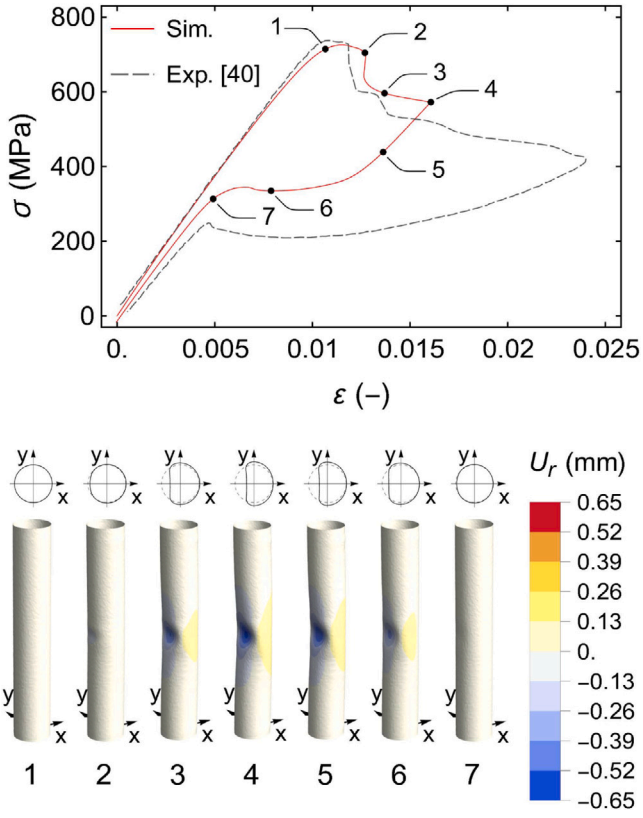


**Fig. 6.** Comparison of the numerical and experimental response in the stress–strain diagram of D2.5&Dt25 tube with $L_g$ = 14 mm that exhibits local buckling with 1 circumferential wave (LB1).

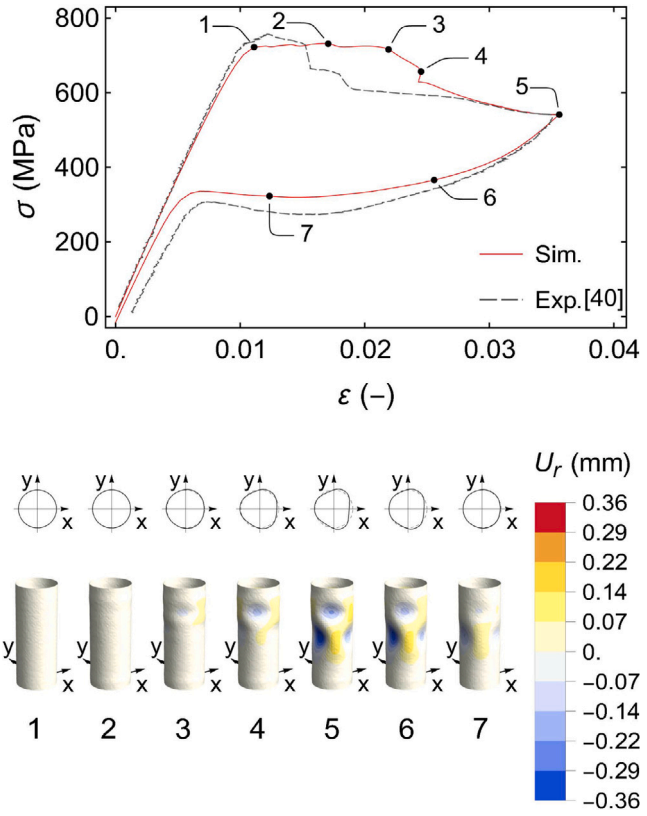


**Fig. 7.** Comparison of the numerical and experimental response in the stress–strain diagram of D2.5&Dt25 tube with $L_g$ = 6 mm that exhibits local buckling with 3 circumferential waves (LB3).

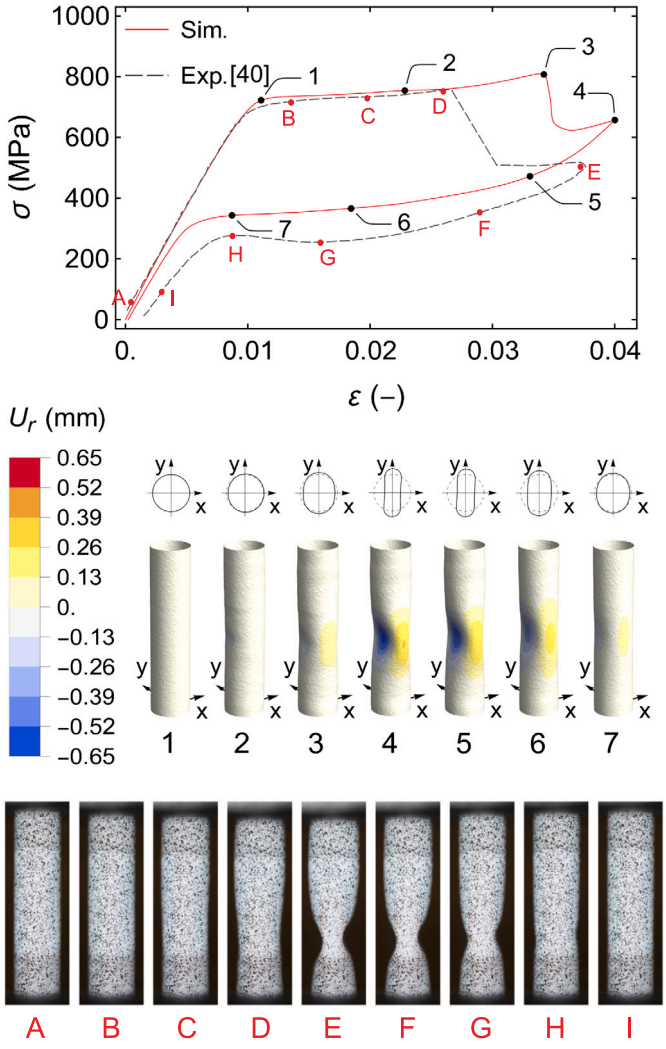


**Fig. 8.** Comparison of the numerical and experimental response in the stress–strain diagram and buckling modes of D2.5&Dt17 tube with $L_g$ = 10 mm that exhibits local buckling with 2 circumferential waves (LB2).

Medium-short and medium-thin tubes, e.g., D2.5&Dt17 with $L_g$ = 10 mm, exhibited local buckling with 2 waves in the circumferential direction, as shown in Fig. 8, where the experimental and numerical responses of the tube are compared. Similar to the LB3 case, the initiation of instabilities occurs at the beginning of the transformation (point 1). As the axial load increases, the cross-section of the tube begins to ovalize until failure (point 3), whereupon the stress decreases and the opposite sides of the wall of the tube buckle towards the center. At point 4, the strain limit $\varepsilon_{\text{lim}} = 0.04$ is reached, and unloading begins. The general trends of the experimental and numerical responses in the diagram match well. Note that the reason for defining the strain limit higher compared to the experiments, i.e., $\varepsilon_{\text{lim}} = 0.04$, is the intention to show well expressed/exhibited buckling mode of the tube.

Short and medium-thin tubes, e.g., D2.5&Dt17 with $L_g$ = 6 mm, exhibit local buckling–unbuckling, as shown in Fig. 9. In contrast to all other buckling modes, the tube starts to exhibit local buckling, i.e., the cross section of the tube starts to ovalize, somewhere in the middle of the transformation (point 3 in Fig. 9). For certain parts of the tube, a further axial load leads to a reduction of the displacements in the lateral direction, i.e., an unbuckling. More specifically, the displacement in the $x$-direction of the material point on the tube with the coordinates $(-D_{\text{mid}}, 0, L_s + L_g/2)$ decreases between point 3 and point 4, event though the stress increases from approximately 800 MPa to 1100 MPa (see the diagram and the zoom-in regions at the bottom of Fig. 9). The displacements at the centers of the small red ellipses are 0.056 mm and 0.052 mm. However, the displacement in the $y$-direction of the material point on the tube with the coordinates $(0, -D_{\text{mid}}, L_s + L_g/2)$ always increases with increasing axial load. Based on this we leave open the possibility that the changes of lateral displacements are a consequence of the transition between different local buckling modes, rather than unbuckling. Nonetheless, there is no failure of the tube. Numerical and experimental curves in the stress–strain diagram fits very well.

Although the experimental and numerical responses of different tubes shown in Figs. 3–9 match quite well, some discrepancies occurred. There are several potential reasons for that. First and already mentioned, is the measurement error after a failure of the tube. Second, the defined boundary conditions in the simulations may not perfectly reflect the actual clamping conditions. Third, our definition of imperfections might not encompass all real imperfections, which in reality orient randomly. And fourth, the assumption of the constitutive equations omits the formation of residual martensite. Note that the second and the third reason contribute to the fact that tubes in numerical simulations are stiffer (compared to the experiments), while the latter reason is responsible for the mismatch of experimental and numerical stress–strain curve at the end of the unloading. Nevertheless and despite these factors, the trend of the numerical responses adequately match the experiments in all cases.

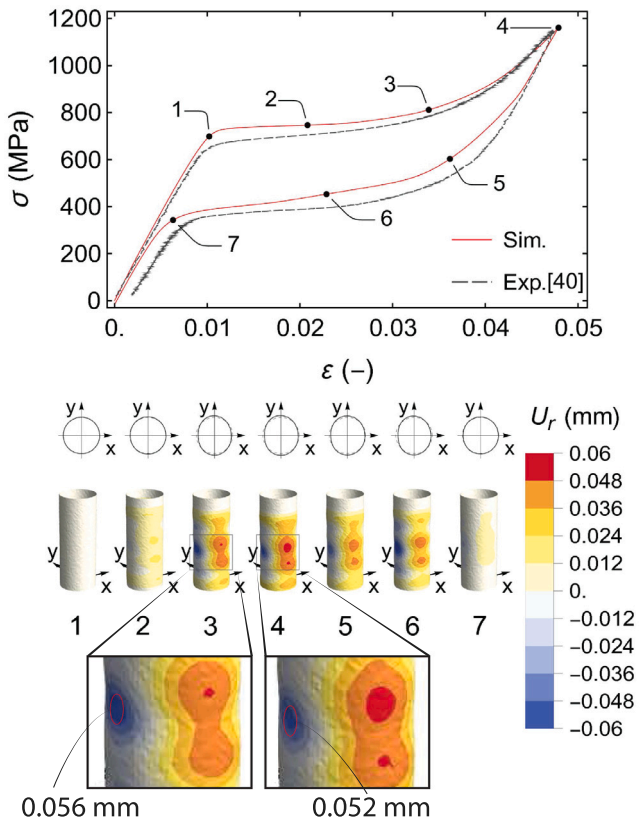


**Fig. 9.** Comparison of the numerical and experimental response in the stress–strain diagram of D2.5&Dt17 tube with $L_g = 6$ mm that exhibits local buckling–unbuckling (LBUB). Zoomed-in regions show two consecutive deformation fields in states at points 3 and 4, where approximately 800 and 1100 MPa of stress and 0.056 and 0.052 mm of radial displacement is found at the center of the red ellipse.

### 4.2. Phase diagrams

Tubes of different lengths with the cross-sections given in Table 1 were considered in our main simulations. Based on these, we created numerical phase diagrams of buckling modes that are compared with the experiments from [40]. Note that the experimental phase diagrams shown in this paper are based on an isothermal loading cycle only and therefore differ from the phase diagrams shown in [40], which are based on buckling modes obtained after 50 training and 20 adiabatic cycles. As explained in [40] in some cases buckling occurred during training or (in rare) cases during adiabatic cycling, which means that in some cases the tubes in the isothermal phase diagrams of buckling modes (see e.g., Fig. 10) seems to be more stable compared to the one after training and adiabatic cycling. Fig. 10 shows experimental and numerical phase diagrams for the tubes with an approximately constant ratio $D_{out}/t = 12$ in $\lambda$-$D_{out}$ space. The slenderness $\lambda$ is defined as

$$\lambda = \frac{L_g}{\sqrt{I/A}}, \quad \text{where} \quad I = \frac{\pi}{64}\left(D_{out}^4 - D_{in}^4\right) \quad \text{and} \quad A = \pi\left(\frac{D_{out}^2}{4} - \frac{D_{out}^2}{4}\right), \tag{34}$$

where $I$ is the second moment of the cross-section and $A$ its area. The thin gray lines in Fig. 10 indicate equal lengths of the tubes, while the circle represents the tube with a specific geometry. The colors inside the circles indicate the buckling modes, while the numbers inside the pie-charted circles (in Fig. 10(a)) indicate the number of tubes that exhibited the respective buckling mode during the experiments. The thick black line in Fig. 10(a) approximately defines the boundary between the areas of buckling modes (GBUB and GB+LB1) in the experimental phase diagram, while the colors in the background define the areas of different buckling modes. On the other hand, a dashed line in Fig. 10(a) represents the boundary between GBUB and GB+LB1 obtained numerically.

All the tubes considered in the simulations exhibited either GBUB or GB+LB1, which is consistent with the experiments. As mentioned in the previous sections, the tubes are slightly stiffer in the simulations than in the experiments (see Fig. 4), which is also reflected in the phase diagram (Fig. 10(b)), where several tubes with slenderness between 20 and 23 exhibit GBUB in the simulation, while GB+LB1 was observed in the experiments. A noticeable difference between the experiments and the simulation lies in the trend of the boundary between GBUB and GB+LB1. In the simulations, the trend seems to be linear (indicated by a dashed line), i.e., as the outer diameter $D_{out}$ increases, the maximal length of the tubes exhibiting GBUB increases. On the other hand, the experimental results show a parabolic trend with a minimum at about $D_{out} = 2.5$ mm. Nevertheless, the difference between experiments and numerical predictions of the length of the tubes that exhibited GBUB is rather small, more specifically, 14.3% for $D_{out} = 2$ mm, 22.2% for $D_{out} = 2.5$ mm, and 18.2% for $D_{out} = 3$ mm. Note that shorter tubes than those considered in the simulations (and experiments) have the same buckling mode as the shortest analyzed tube with the given cross-section.

Fig. 11 shows experimental and numerical phase diagrams for the tubes of the constant $D_{out} = 2.5$ mm in the $\lambda$-$D_{out}/t$ space. Similar to Fig. 10, areas of buckling modes and the boundaries between them are defined in the experimental phase diagram and are also shown in the numerical phase diagram to facilitate comparison between them.

In Fig. 11(a) at the bottom left-hand side of the phase diagram, there is an area where GBUB is prevalent. Increasing the length of the D2.5&Dt5 tube to 18 mm (and above) leads to GB, i.e., failure. Tubes with a higher $D_{out}/t$ ratio (up to $D_{out}/t = 12$) fail (GB+LB1) at even shorter lengths, i.e., $L_g \approx 16$ mm. At the bottom right-hand side of the diagram (at $D_{out}/t > 15$), there is an area in which local buckling modes are prevalent. The D2.5&Dt17 tubes mainly exhibit LB2, with the exception of one tube of $L_g = 6$ mm, which showed LBUB and did not fail during the isothermal loading cycle. In contrast, D2.5&Dt25 tubes exhibited LB2 and LB3 at shorter lengths ($L_g \leq 10$ mm), as well as LB1, which is prevalent in tubes with $L_g$ between 10 and 14 mm. Based on the obtained results, it is assumed that tubes that are longer than those considered in the experiments and have a ratio of $D_{out}/t \geq 10$ exhibit GB+LB1, hence the upper right-hand side part of the diagram is colored red. Note that there is a white triangle bounded by dashed lines in the center of the experimental phase diagram indicating that the buckling mode is unknown.

Fig. 11(b) shows an experimentally determined phase diagram from Fig. 11(a), in which colored circles represent different numerically determined buckling modes are plotted over for easier comparison of the two approaches. More specifically, D2.5&Dt10 and D2.5&Dt12 tubes that exhibit GBUB are longer compared to the experiments, while D2.5&Dt5 tubes of $L_g = 18$ mm exhibit GB in both cases. The overestimation of the length of the tubes that exhibit GBUB is about 16% for D2.5&Dt10 and D2.5&Dt12 tubes. The reason for this discrepancy is the higher stiffness of the tubes in the simulations as already mentioned above. For the same reason, D2.5&Dt17 tube of $L_g \leq 8$ mm exhibit LBUB (based on simulations), while LB2 was prevalent in the experiments. For the D2.5&Dt17 tube of $L_g = 14$ mm, the dominant buckling mode is GB+LB1 in the experiments and simulations. There is also a good agreement between numerical and experimental results for D2.5&Dt25 tubes, where LB3, LB2, and LB1 are observed in both cases. In the simulations, a transition from LB3 to LB2 and finally to LB1 with increasing length of the tube is observed for those tubes, while this transition is not distinctive in the experiments. It should be noted that for longer tubes the lower buckling eigenmodes are dominant, i.e. LB1, which have longer half-wave length. Shorter tubes, on the other hand,

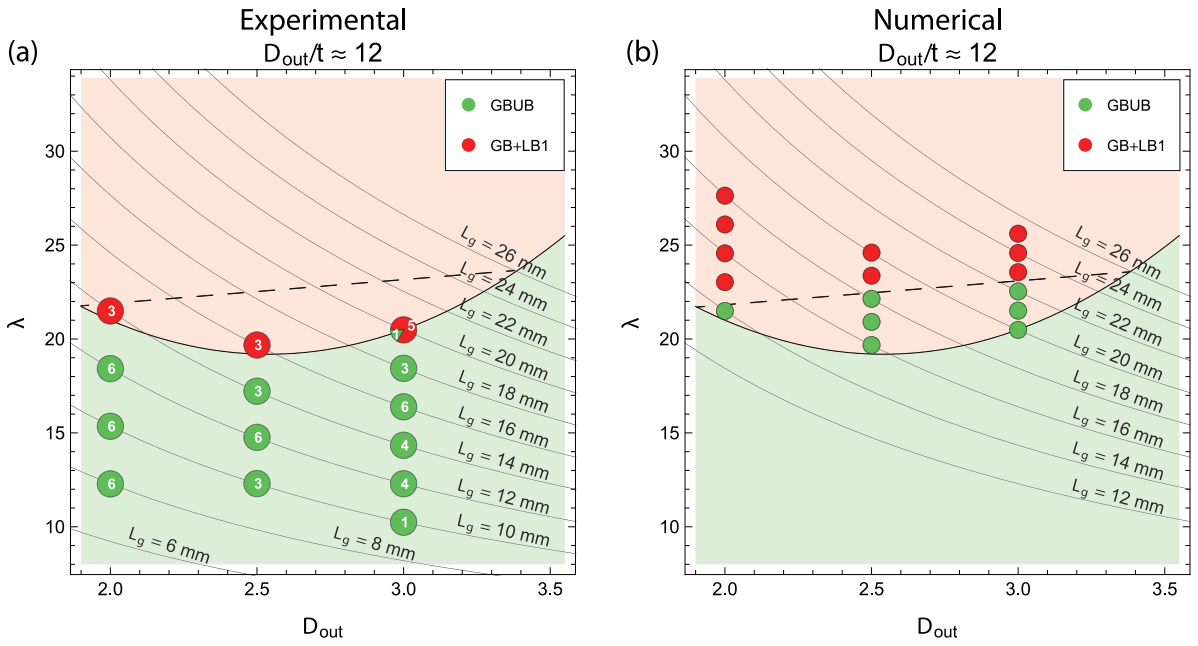


**Fig. 10.** Isothermal phase diagram of buckling modes with marked experimental characteristic areas for the tubes of approximately constant ratio $D_{out}/t = 12$ in $\lambda$-$D_{out}$ space: (a) experimental and (b) numerical.

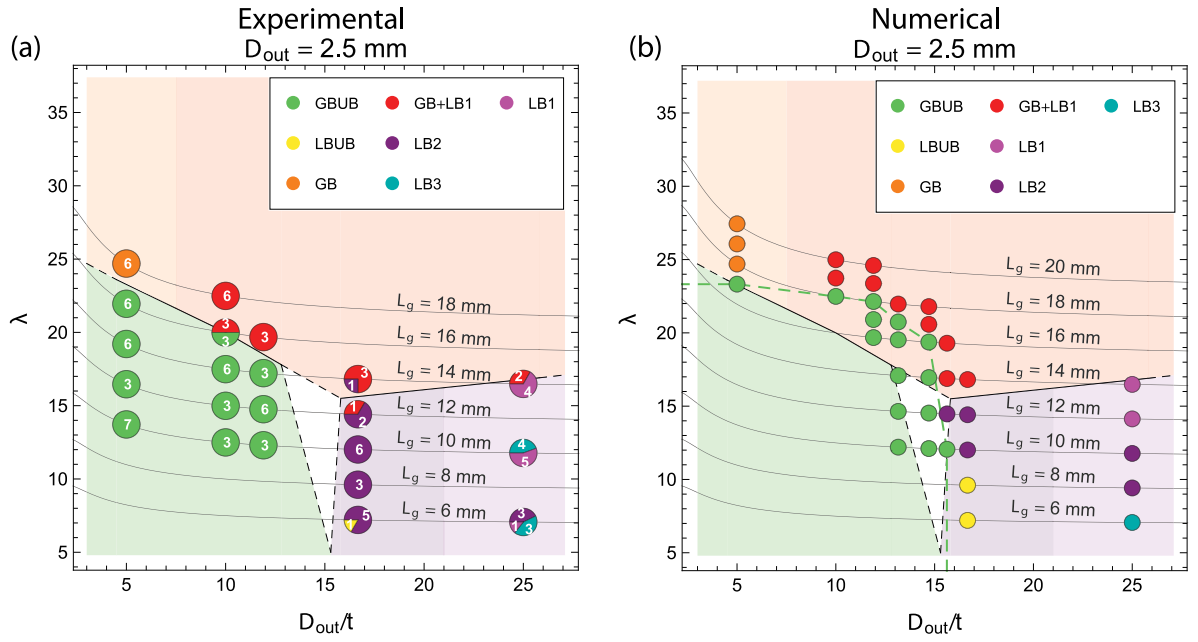


**Fig. 11.** Isothermal phase diagram of buckling modes with marked experimental characteristic areas for the tubes of constant $D_{out} = 2.5$ mm in $\lambda$-$D_{out}/t$ space: (a) experimental and (b) numerical.

allow buckling eigenmodes with shorter half-wave length (e.g. LB3). Note that a green dashed line, which defines a boundary between GBUB and GB+LB1 obtained numerically, is shown in the numerical phase diagram only (Fig. 11(b)) for easier compassion of the areas where GBUB is prevalent for tubes with different $D_{out}$ (see Fig. 12).

In order to close the gap in the experimental phase diagram between $D_{out}/t = 12$ and $D_{out}/t = 17$ additional tubes were included in the simulations, namely, D2.5&Dt13, D2.5&Dt15, and D2.5&Dt16. One can see that maximum $L_g$ that exhibit GBUB decreases from $L_g = 17$ mm to $L_g = 16$ mm and $L_g = 10$ mm when $D_{out}/t$ increases from 13 to 15 and 16, respectively. Interestingly, the D2.5&Dt16 tube shows an unusual transition from GBUB to GB+LB1, between which LB2 is observed (at $L_g = 12$ mm). This could be the case for all tubes. However, the step length of the observed tubes should have been smaller.

Fig. 12 shows the numerical phase diagrams of buckling modes for tubes of $D_{out} = 2$ and $D_{out} = 3$ mm. The locations of the GBUB area are comparable in all numerical diagrams, especially for the tubes with $D_{out}/t = 5$, while some deviation is observed for tubes with $D_{out}/t \approx 13$. Moreover, slenderness $\lambda$ of the longest tubes (with identical $D_{out}/t$ ratio

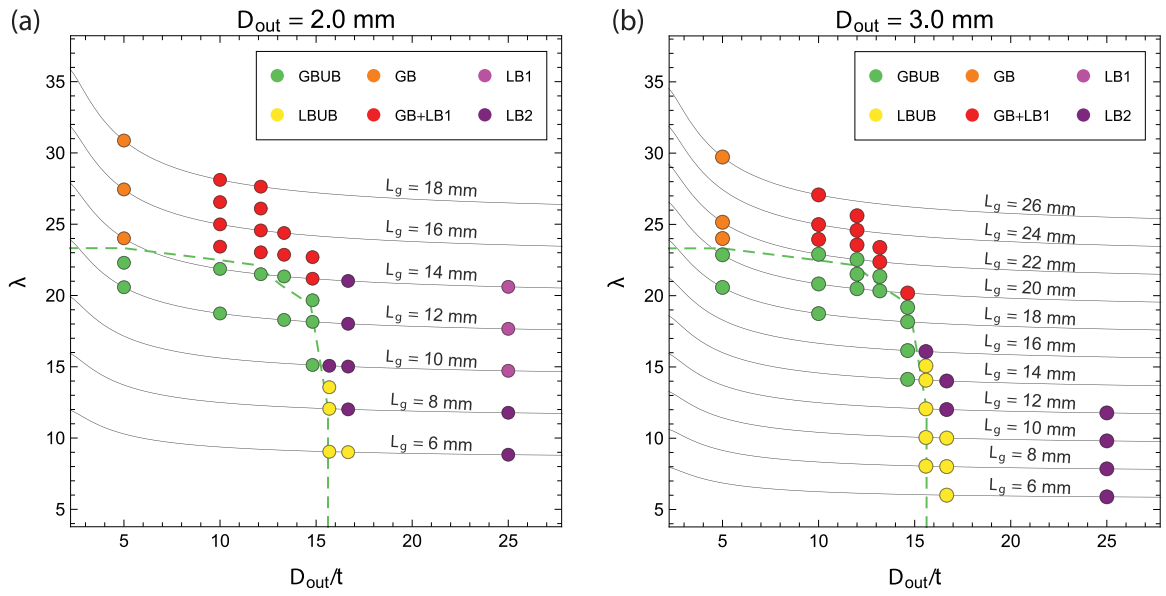


**Fig. 12.** Numerical isothermal phase diagram of buckling modes with marked area of GBUB for the tubes of constant $D_{out}$ in $\lambda$-$D_{out}/t$ space: (a) $D_{out}$ = 2.0 mm and (b) $D_{out}$ = 3.0 mm.

and different $D_{out}$) exhibiting GBUB is almost identical for all considered $D_{out}$, while the length $L_g$ changes significantly. This indicates that $\lambda$ is a good choice of dimensionless parameter for use in the phase diagram. Note that other parts of the numerical phase diagrams also agree well, e.g., the buckling mode of longer tubes with $D_{out}/t = 5$ exhibit GB, while tubes of $D_{out}/t \geq 15$ show GB+LB1.

The main difference between numerically obtained phase diagrams of the tubes with different outer diameters is in the local buckling area, where interestingly, D2&Dt25 and D3&Dt25 tubes do not exhibit LB3 for any of the lengths considered. One of the reasons for that could be the selection of amplitudes $A_f$ and $A_m$, which can affect exhibited buckling mode of the tube as pointed out in Appendix A (see Table A.1). Furthermore, they might differently affect the tubes with different $D_{out}$. Furthermore, for tubes with $D_{out}$ = 3 mm, LB2 is significantly more common compared to the tubes with lower $D_{out}$. This leads to the conclusion that tubes with larger $D_{out}$ at the boundary between GBUB and local buckling area tend to exhibit LBUB rather than GBUB. Another interesting observation is that tubes of $D_{out}/t = 25$ with $\lambda < 13$ prevalently exhibit LB2 for all outer diameters of the tubes considered (2, 2.5, and 3 mm).

## 5. Conclusions

In this work, shell finite elements were used for the first time to investigate the buckling of SMA tubes that are subjected to axial compressive loading. More specifically, the 7-parameter shell finite element, which is based on finite strain theory and allows direct implementation of 3D constitutive equations, was used to predict the mechanical response of tubes of various dimensions. In particular, we considered tubes with outer diameter $D_{out}$ between 2 and 3 mm, ratio $D_{out}/t$ between 5 and 25, and gauge length $L_g$ between 6 and 26 mm, which are particularly interesting for elastocaloric applications.

Special attention was devoted to the definition of the imperfection that breaks the symmetry of the tube in the numerical simulations (in which the geometry is usually defined as ideal) and causes the potential initiation of instability. In order to predict various buckling modes that are exhibited by various tubes, a combination of two types of imperfections was implemented, namely, a random perturbation of the mesh in the radial direction and a lateral perturbation force in the center of the tube. The randomness of the first ensures that the response of the tube is not prejudiced into the specific buckling mode, while the second is used to decrease the overall stiffness of the tube. The amplitude of each imperfection was determined in the sensitivity analysis (See Appendix A) by comparing the numerical response of the tubes to the experimental observations from [40].

Tubes of different dimensions exhibited different responses and several buckling modes were observed and identified numerically. These are global buckling–unbuckling (GBUB), global buckling (GB), a combination of global and local (snap-through) buckling (GB+LB1), local buckling–unbuckling (LBUB), local buckling with 1 circumferential wave (LB1), local buckling with 2 circumferential waves (LB2), and local buckling with 3 circumferential waves (LB3). Numerical responses of the tubes were compared to the experiments in [40] in stress–strain diagrams as well as phase diagrams of buckling modes. We showed that the agreement between numerical and experimental stress–strain curves is very good. However, it was observed that the tubes in numerical simulations are, to a certain extent, stiffer compared to the experiments (the main reason for that being the definition of imperfection in our model and assumptions of the constitutive equations). Despite this, the buckling modes that were observed in simulations and experiments agree very well for the majority of the considered tubes. The comparison of buckling modes was performed by comparing two types of isothermal phase diagrams of buckling modes. First, for the tubes of approximately constant $D_{out}/t = 12$ in $\lambda$-$D_{out}$ space and second, for tubes of constant $D_{out}$ = 2.5 mm in $\lambda$-$D_{out}/t$ space. Furthermore, two additional numerical phase diagrams were also created for tubes of constant $D_{out}$ = 2 mm and $D_{out}$ = 3 mm in $\lambda$-$D_{out}/t$ space. We observed that the transition from GBUB to failure (GB or GB+LB1) for $D_{out}/t \leq 12$ is at $\lambda \approx 22.5$ and almost independent of $D_{out}$. Similarly, independent of $D_{out}$, the transition from GBUB to LBUB (which is also considered a failure) is at $D_{out}/t \approx 15.5$. In the region of $12 \leq D_{out}/t \leq 15.5$, the slenderness of the tubes that exhibit GBUB drastically decreases towards 0. Based on this, we conclude that $\lambda$ and $D_{out}/t$ are appropriate parameters for defining the phase diagrams and comparison of buckling modes between tubes of different $D_{out}$. It must be emphasized that tubes with geometry inside the GBUB region on the phase diagrams have the potential to be used in practical elastocaloric applications since they can be considered as functionally stable, see [40].

To summarize, in this work we verified our numerical model [42] by comparing the results to the experiments [40]. Therefore, the confidence in the prediction of instability of tubes is increased, and we assess that the developed simulation model presents an important tool for a

**Table A.1**
Buckling modes of D2.5&Dt25 tube with $L_g = 6$ mm for various amplitudes of mesh and force perturbations.

| | $A_f = 0\%$ | $A_f = 0.01\%$ | $A_f = 0.05\%$ | $A_f = 0.1\%$ | $A_f = 0.15\%$ |
|---|---|---|---|---|---|
| $A_m = 0.5\%$ | LB3 | random LB2 | LB2 | LB2 | LB2 |
| $A_m = 1\%$ | LB3 | LB3 | random LB2 | LB2 | LB2 |
| $A_m = 2\%$ | LB3 | LB3 | random LB2 | LB2 | LB2 |
| $A_m = 3\%$ | LB3 | LB3 | LB3 | LB3 | LB2 |

reliable and fast design of SMA elements for elastocaloric technology. In the future we will be able to investigate buckling of various more advanced SMA elements and structures (e.g., square tube, ribbed plate, curved plate, wavy plate) using this numerical approach.

## CRediT authorship contribution statement

**Luka Porenta:** Writing – original draft, Software, Investigation, Formal analysis, Data curation, Conceptualization. **Boštjan Brank:** Writing – review & editing, Supervision, Software, Investigation, Formal analysis. **Jaka Tušek:** Writing – review & editing, Writing – original draft, Supervision, Resources, Methodology, Investigation, Funding acquisition, Conceptualization. **Miha Brojan:** Writing – review & editing, Writing – original draft, Visualization, Validation, Supervision, Methodology, Investigation, Conceptualization.

## Declaration of competing interest

The authors declare that they have no known competing financial interests or personal relationships that could have appeared to influence the work reported in this paper.

## Acknowledgments

This work was supported by European Research Council under Horizon 2020 program (ERC Starting Grant No. 803669).

## Appendix A. Sensitivity analysis about multiple random meshes of identical geometry

A sensitivity analysis was performed to determine which combination of force and mesh perturbation amplitudes, $A_f$ and $A_m$ respectively, gave the most realistic results, i.e., a response most comparable to the experiments. Five different amplitudes of force perturbation (0, 0.01, 0.05, 0.1, and 0.15%) and four different amplitudes of mesh perturbation (0.5, 1, 2, and 3%) were considered in the analysis. Due to the randomized mesh perturbation, each combination of perturbation amplitudes was considered five times. With this approach, the general response of the tube was verified, which means that the buckling mode is independent of the randomness of mesh perturbation (with constant force perturbation), while the direction of buckling is the consequence of the randomness. In other words, identical buckling modes were observed in all five cases of the considered combination of perturbations. Different dimensions of the tube were considered in this analysis, i.e., D2.5&Dt25 tube with $L_g = 6$ mm, D2.5&Dt5 tube with $L_g = 18$ mm, D2.5&Dt12 tube with $L_g = 16$ mm, and D2.5&Dt25 tube with $L_g = 14$ mm. The results for the D2.5&Dt25 tube with $L_g = 6$ mm are summarized in Table A.1, while the rest is summarized in Tables A.2–A.4.

As expected, the D2.5&Dt25 tube with $L_g = 6$ mm exhibited local buckling, i.e., LB2 and LB3. Labels containing "random" indicate that buckling occurred in any direction (as a consequence of the randomness of the mesh perturbation), regardless of the direction of the force perturbation. This means that the amplitude of the perturbation force is large enough to influence the buckling mode, while the effect of the mesh perturbation is not negligible. At low $A_f$ and high $A_m$, LB3 is prevalent for D2.5&Dt25 tubes with $L_g = 6$ mm, while higher $A_f$ at lower $A_m$ leads to LB2. Considering the transition from LB3 to LB2 with a random LB2 buckling mode in between, it can be concluded that the higher the amplitude of the mesh perturbation, the higher the amplitude of the perturbation force needed to counteract the randomness of the mesh perturbation.

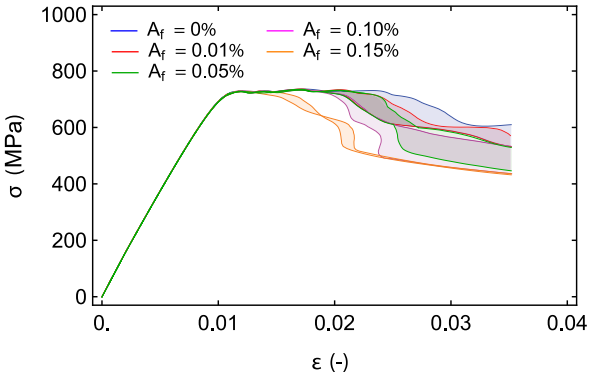


**Fig. A.1.** Comparison of buckling response of D2.5&Dt25 tubes with $L_g = 6$ mm subjected to various perturbation force amplitudes $A_f$.

In other cases, there is no transition from one buckling mode to another, when various amplitudes of the perturbation are considered. However, two trends are noticeable. First, the higher the amplitude $A_m$, the higher perturbation force is required to counteract the randomness of the mesh perturbation, e.g., higher $A_f$ results in GB instead of random GB (Table A.2). Second, the thicker the tube, the higher perturbation force is required to dominate over random mesh perturbation, e.g., at $A_m = 3$ % the amplitude $A_f = 0.05\%$ is enough for D2.5&Dt25 tube (Table A.4), while D2.5&Dt12 tube requires $A_f = 0.1\%$ (Table A.3) and for D2.5&Dt5 amplitude $A_f = 0.15\%$ is not enough (Table A.2).

In Fig. A.1, the responses of D2.5&Dt25 tubes with $L_g = 6$ mm are shown in the stress–strain diagram. For each force amplitude $A_f$ a region of possible paths is marked, while the specific curve within the region is dependent on the amplitude of the mesh perturbation $A_m$. The effect of the force perturbation amplitude is clearly visible, i.e., at higher force perturbation amplitudes, the values of strain at which the curve starts to decline are lower. On the other hand, the effect of mesh perturbation amplitude is visible in the response of the tube after the occurrence of instability. More specifically, it affects the path of the curve. However, the trend is not noticeable. Note that the relatively wide region for the case of $A_f = 0.10\%$ is a consequence of the noticeable transition from LB2 to LB3 with increasing the mesh perturbation amplitude.

For selecting the right combination of mesh and force perturbation amplitudes, two criteria were considered. First, the buckling mode in the simulations should match the buckling mode that was observed during the experiments, e.g., LB3 for D2.5&Dt25 tube with $L_g = 6$ mm. Second, the tangent modulus of the elastic response of the tube in the simulations should match the experiments as much as possible in the stress–strain diagram, indicating that the stiffness of the tube is comparable in both cases. Based on the sensitivity analysis, $A_m = 3$ % and $A_f = 0.1$ % are the most appropriate values to obtain the most realistic results. Therefore, these amplitudes were used in the simulations, which served as a base for constructing the phase diagrams.

**Table A.2**
Buckling modes of D2.5&Dt5 tube with $L_g$ = 18 mm for various amplitudes of mesh and force perturbations.

| | $A_f$ = 0% | $A_f$ = 0.01% | $A_f$ = 0.05% | $A_f$ = 0.1% | $A_f$ = 0.15% |
|---|---|---|---|---|---|
| $A_m$ = 0.5% | random GB | random GB | GB | GB | GB |
| $A_m$ = 1% | random GB | random GB | GB | GB | GB |
| $A_m$ = 2% | random GB | random GB | random GB | GB | GB |
| $A_m$ = 3% | random GB | random GB | random GB | random GB | random GB |

**Table A.3**
Buckling modes of D2.5&Dt12 tube with $L_g$ = 16 mm for various amplitudes of mesh and force perturbations.

| | $A_f$ = 0% | $A_f$ = 0.01% | $A_f$ = 0.05% | $A_f$ = 0.1% | $A_f$ = 0.15% |
|---|---|---|---|---|---|
| $A_m$ = 0.5% | random GBUB | GBUB | GBUB | GBUB | GBUB |
| $A_m$ = 1% | random GBUB | random GBUB | GBUB | GBUB | GBUB |
| $A_m$ = 2% | random GBUB | random GBUB | GBUB | GBUB | GBUB |
| $A_m$ = 3% | random GBUB | random GBUB | random GBUB | GBUB | GBUB |

**Table A.4**
Buckling modes of D2.5&Dt25 tube with $L_g$ = 14 mm for various amplitudes of mesh and force perturbations.

| | $A_f$ = 0% | $A_f$ = 0.01% | $A_f$ = 0.05% | $A_f$ = 0.1% | $A_f$ = 0.15% |
|---|---|---|---|---|---|
| $A_m$ = 0.5% | random LB1 | LB1 | LB1 | LB1 | LB1 |
| $A_m$ = 1% | random LB1 | LB1 | LB1 | LB1 | LB1 |
| $A_m$ = 2% | random LB1 | random LB1 | LB1 | LB1 | LB1 |
| $A_m$ = 3% | random LB1 | random LB1 | LB1 | LB1 | LB1 |

## Data availability

Data will be made available on request.

## References


[1] J.M. Jani, M. Leary, A. Subic, M.A. Gibson, A review of shape memory alloy research, applications and opportunities, Mater. Des. (1980–2015) 56 (2014) 1078–1113.

[2] L. Petrini, F. Migliavacca, Biomedical applications of shape memory alloys, J. Metall. 2011 (2011).

[3] G. Costanza, M.E. Tata, Shape memory alloys for aerospace, recent developments, and new applications: A short review, Materials 13 (8) (2020) 1856.

[4] W. Coral, C. Rossi, J. Colorado, D. Lemus, A. Barrientos, SMA-based muscle-like actuation in biologically inspired robots: A state of the art review, in: Smart Actuation Sensing Systems-Recent Advances and Future Challenges, IntechOpen, 2012, pp. 53–82.

[5] O. Ozbulut, S. Hurlebaus, R. Desroches, Seismic response control using shape memory alloys: A review, J. Intell. Mater. Syst. Struct. 22 (14) (2011) 1531–1549.

[6] N.C. Inc., Energy savings potential and RD&D opportunities for non-vapor-compression HVAC technologies, 2014, http://dx.doi.org/10.2172/1220817, URL https://www.osti.gov/biblio/1220817.

[7] VHK, ARMINES, Technology roadmap in preparatory/review study on commission regulation (EC) no. 643/2009 with regard to ecodesign requirements for household refrigeration appliances and commission delegated regulation (EU) no. 1060/2010 with regard to energy labelling, 2016, www.ecodesign-fridges.eu.

[8] P. Kabirifar, A. Žerovnik, Ž. Ahčin, L. Porenta, M. Brojan, J. Tušek, Elastocaloric cooling: State-of-the-art and future challenges in designing regenerative elastocaloric devices, Strojniski Vestnik/J. Mech. Eng. 65 (2019).

[9] J. Tušek, K. Engelbrecht, D. Eriksen, S. Dall'Olio, J. Tušek, N. Pryds, A regenerative elastocaloric heat pump, Nat. Energy 1 (10) (2016) 1–6.

[10] S. Qian, Y. Geng, Y. Wang, J. Muehlbauer, J. Ling, Y. Hwang, R. Radermacher, I. Takeuchi, Design of a hydraulically driven compressive elastocaloric cooling system, Sci. Technol. Built Environ. 22 (5) (2016) 500–506.

[11] R. Snodgrass, D. Erickson, A multistage elastocaloric refrigerator and heat pump with 28 K temperature span, Sci. Rep. 9 (1) (2019) 1–10.

[12] G. Ulpiani, F. Bruederlin, R. Weidemann, G. Ranzi, M. Santamouris, M. Kohl, Upscaling of SMA film-based elastocaloric cooling, Appl. Therm. Eng. 180 (2020) 115867.

[13] F. Greibich, R. Schwödiauer, G. Mao, D. Wirthl, M. Drack, R. Baumgartner, A. Kogler, J. Stadlbauer, S. Bauer, N. Arnold, et al., Elastocaloric heat pump with specific cooling power of 20.9 W $g^{-1}$ exploiting snap-through instability and strain-induced crystallization, Nat. Energy 6 (3) (2021) 260–267.

[14] N. Bachmann, A. Fitger, L.M. Maier, A. Mahlke, O. Schäfer-Welsen, T. Koch, K. Bartholomé, Long-term stable compressive elastocaloric cooling system with latent heat transfer, Commun. Phys. 4 (1) (2021) 1–6.

[15] L. Ianniciello, K. Bartholomé, A. Fitger, K. Engelbrecht, Long life elastocaloric regenerator operating under compression, Appl. Therm. Eng. 202 (2022) 117838.

[16] Ž. Ahčin, S. Dall'Olio, A. Žerovnik, U.Ž. Baškovič, L. Porenta, P. Kabirifar, J. Cerar, S. Zupan, M. Brojan, J. Klemenc, et al., High-performance cooling and heat pumping based on fatigue-resistant elastocaloric effect in compression, Joule 6 (10) (2022) 2338–2357.

[17] S. Qian, D. Catalini, J. Muehlbauer, B. Liu, H. Mevada, H. Hou, Y. Hwang, R. Radermacher, I. Takeuchi, High-performance multimode elastocaloric cooling system, Science 380 (6646) (2023) 722–727.

[18] G. Zhou, Y. Zhu, S. Yao, Q. Sun, Giant temperature span and cooling power in elastocaloric regenerator, Joule 7 (9) (2023) 2003–2015.

[19] H. Hou, J. Cui, S. Qian, D. Catalini, Y. Hwang, R. Radermacher, I. Takeuchi, Overcoming fatigue through compression for advanced elastocaloric cooling, MRS Bull. 43 (4) (2018) 285–290.

[20] J. Tušek, A. Žerovnik, M. Čebron, M. Brojan, B. Žužek, K. Engelbrecht, A. Cadelli, Elastocaloric effect vs fatigue life: Exploring the durability limits of Ni-Ti plates under pre-strain conditions for elastocaloric cooling, Acta Mater. 150 (2018) 295–307.

[21] J. Chen, K. Zhang, Q. Kan, H. Yin, Q. Sun, Ultra-high fatigue life of NiTi cylinders for compression-based elastocaloric cooling, Appl. Phys. Lett. 115 (9) (2019) 093902.

[22] L. Porenta, P. Kabirifar, A. Žerovnik, M. Čebron, B. Žužek, M. Dolenec, M. Brojan, J. Tušek, Thin-walled Ni-Ti tubes under compression: ideal candidates for efficient and fatigue-resistant elastocaloric cooling, Appl. Mater. Today 20 (2020) 100712.

[23] Y. Urushiyama, D. Lewinnek, J. Qiu, J. Tani, Buckling of curved column and twinning deformation effect, in: IUTAM Symposium on Smart Structures and Structronic Systems, Springer, 2001, pp. 283–290.

[24] M.A. Rahman, J. Qiu, J. Tani, Buckling and postbuckling characteristics of the superelastic SMA columns, Int. J. Solids Struct. 38 (50–51) (2001) 9253–9265.

[25] Y. Urushiyama, D. Lewinnek, J. Qiu, J. Tani, Buckling of shape memory alloy columns, JSME Int. J. Ser. A Solid Mech. Mater. Eng. 46 (1) (2003) 60–67.

[26] M.A. Rahman, J. Qiu, J. Tani, Buckling and postbuckling characteristics of the superelastic SMA columns – Numerical simulation, J. Intell. Mater. Syst. Struct. 16 (9) (2005) 691–702.

[27] F. Richter, O. Kastner, G. Eggeler, Finite-element simulation of the anti-buckling-effect of a shape memory alloy bar, J. Mater. Eng. Perform. 20 (4) (2011) 719–730.

[28] J. Pereiro-Barceló, J.L. Bonet, Ni-Ti SMA bars behaviour under compression, Constr. Build. Mater. 155 (2017) 348–362.

[29] R.T. Watkins, B. Reedlunn, S. Daly, J.A. Shaw, Uniaxial, pure bending, and column buckling experiments on superelastic NiTi rods and tubes, Int. J. Solids Struct. 146 (2018) 1–28.

[30] A.M. Asfaw, M.M. Sherif, G. Xing, O.E. Ozbulut, Experimental investigation on buckling and post-buckling behavior of superelastic shape memory alloy bars, J. Mater. Eng. Perform. 29 (5) (2020) 3127–3140.

[31] S. Suzuki, Y. Urushiyama, M. Taya, Energy absorption material using buckling strength of shape memory alloy plate, in: Smart Structures and Materials 2004: Active Materials: Behavior and Mechanics, vol. 5387, International Society for Optics and Photonics, 2004, pp. 218–227.

[32] S. Nemat-Nasser, J.Y. Choi, J.B. Isaacs, D.W. Lischer, Quasi-static and dynamic buckling of thin cylindrical shape-memory shells, J. Appl. Mech. 73 (5) (2006) 825–833.

[33] Z. Tang, D. Li, Experimental investigation of axial impact buckling response of pseudo-elastic NiTi cylindrical shells, Int. J. Impact Eng. 39 (1) (2012) 28–41.
[34] Z. Tang, D. Li, Quasi-static axial buckling behavior of NiTi thin-walled cylindrical shells, Thin-Walled Struct. 51 (2012) 130–138.
[35] R. Watkins, Thermomechanical Characterization and Modeling of Superelastic Shape Memory Alloy Beams and Frames (Ph.D. thesis), University of Michigan, 2015.
[36] D. Jiang, N.J. Bechle, C.M. Landis, S. Kyriakides, Buckling and recovery of NiTi tubes under axial compression, Int. J. Solids Struct. 80 (2016) 52–63.
[37] D. Jiang, C.M. Landis, S. Kyriakides, Effects of tension/compression asymmetry on the buckling and recovery of NiTi tubes under axial compression, Int. J. Solids Struct. 100 (2016) 41–53.
[38] A. Damanpack, M. Bodaghi, W. Liao, Snap buckling of NiTi tubes, Int. J. Solids Struct. 146 (2018) 29–42.
[39] Y. Xiao, D. Jiang, Buckling and unbuckling of superelastic NiTi tube, Acta Mech. Solida Sin. (2022) 1–14.
[40] L. Porenta, J. Trojer, M. Brojan, J. Tušek, Experimental investigation of buckling stability of superelastic Ni-Ti tubes under cyclic compressive loading: Towards defining functionally stable tubes for elastocaloric cooling, Int. J. Solids Struct. 256 (2022) 111948.
[41] R.T. Watkins, J.A. Shaw, Unbuckling of superelastic shape memory alloy columns, J. Intell. Mater. Syst. Struct. 29 (7) (2018) 1360–1378.
[42] L. Porenta, M. Lavrenčič, J. Dujc, M. Brojan, J. Tušek, B. Brank, Modeling large deformations of thin-walled SMA structures by shell finite elements, Commun. Nonlinear Sci. Numer. Simul. 101 (2021) 105897.
[43] D. Jiang, C.M. Landis, A constitutive model for isothermal pseudoelasticity coupled with plasticity, Shape Memory Superelasticity 2 (4) (2016) 360–370.
[44] L. Porenta, B. Brank, J. Dujc, M. Brojan, J. Tušek, A shell finite element model for superelasticity of shape memory alloys, in: Analysis of Shells, Plates, and Beams, Springer, 2020, pp. 373–388.
[45] P. Betsch, E. Stein, An assumed strain approach avoiding artificial thickness straining for a non-linear 4-node shell element, Commun. Numer. Methods Eng. 11 (11) (1995) 899–909.
[46] B. Brank, J. Korelc, A. Ibrahimbegović, Nonlinear shell problem formulation accounting for through-the-thickness stretching and its finite element implementation, Comput. Struct. 80 (9–10) (2002) 699–717.
[47] B. Brank, Nonlinear shell models with seven kinematic parameters, Comput. Methods Appl. Mech. Engrg. 194 (21–24) (2005) 2336–2362.
[48] B. Brank, A. Ibrahimbegovic, U. Bohinc, On prediction of 3D stress state in elastic shell by higher-order shell formulations, CMES Comput. Model. Eng. Sci. 33 (1) (2008) 85–108.
[49] B. Brank, D. Perić, F.B. Damjanić, On large deformations of thin elasto-plastic shells: implementation of a finite rotation model for quadrilateral shell element, Internat. J. Numer. Methods Engrg. 40 (4) (1997) 689–726.
[50] B. Brank, A. Ibrahimbegovic, On the relation between different parametrizations of finite rotations for shells, Eng. Comput. (2001).
[51] A. Ibrahimbegovic, B. Brank, P. Courtois, Stress resultant geometrically exact form of classical shell model and vector-like parameterization of constrained finite rotations, Internat. J. Numer. Methods Engrg. 52 (11) (2001) 1235–1252.
[52] A. Ibrahimbegovic, Nonlinear Solid Mechanics: Theoretical Formulations and Finite Element Solution Methods, vol. 160, Springer Science & Business Media, 2009.
[53] J. Korelc, S. Stupkiewicz, Closed-form matrix exponential and its application in finite-strain plasticity, Internat. J. Numer. Methods Engrg. 98 (13) (2014) 960–987.
[54] B. Hudobivnik, J. Korelc, Closed-form representation of matrix functions in the formulation of nonlinear material models, Finite Elem. Anal. Des. 111 (2016) 19–32.
[55] J. Korelc, P. Wriggers, Automation of Finite Element Methods, Springer, 2016.